Bull Math Biol (2013) 75:393–427
DOI 10.1007/s11538-013-9810-0

Society for Mathematical Biology

ORIGINAL ARTICLE

Mathematical Model of Growth Factor Driven Haptotaxis and Proliferation in a Tissue Engineering Scaffold

J.V. Pohlmeyer · S.L. Waters · L.J. Cummings

Received: 1 October 2012 / Accepted: 7 January 2013 / Published online: 29 January 2013
© Society for Mathematical Biology 2013

Abstract Motivated by experimental work (Miller et al. in Biomaterials 27(10):2213–2221, 2006, 32(11):2775–2785, 2011) we investigate the effect of growth factor driven haptotaxis and proliferation in a perfusion tissue engineering bioreactor, in which nutrient-rich culture medium is perfused through a 2D porous scaffold impregnated with growth factor and seeded with cells. We model these processes on the timescale of cell proliferation, which typically is of the order of days. While a quantitative representation of these phenomena requires more experimental data than is yet available, qualitative agreement with preliminary experimental studies (Miller et al. in Biomaterials 27(10):2213–2221, 2006) is obtained, and appears promising. The ultimate goal of such modeling is to ascertain initial conditions (growth factor distribution, initial cell seeding, etc.) that will lead to a final desired outcome.

Keywords Perfusion based bioreactor · Haptotaxis tissue engineering

1 Introduction

Tissue engineering is a relatively young field, yet one whose importance cannot be overstated. There is a shortage of available organs for those in need of transplants

Electronic supplementary material The online version of this article (doi:10.1007/s11538-013-9810-0) contains supplementary material, which is available to authorized users.

J.V. Pohlmeyer · L.J. Cummings (✉)
Department of Mathematical Sciences, New Jersey Institute of Technology, University Heights, Newark, NJ 07102, USA
e-mail: linda.cummings@njit.edu

S.L. Waters
Oxford Centre for Industrial and Applied Mathematics, Oxford Centre for Collaborative Applied Mathematics, University of Oxford, 24–29 St Giles', Oxford, OX1 3LB, UK

(Curtis and Riehle 2001), and the situation will worsen as the world's population continues to increase and age. Many different tissue engineering protocols have been and continue to be researched to determine if it is possible to grow tissue to implant into a patient. In an ideal situation, it would be desirable to harvest an individual's own cells, grow the specific type of tissue needed outside the body, and then re-implant when the tissue is viable. This method of in vitro tissue engineering using the patient's own tissue greatly reduces the risk of tissue rejection. Conducting a large suite of experiments in which tissue is grown within the laboratory undoubtedly provides the best indicator of likely success; however, the time taken for tissue to grow, the "trial and error" nature of optimizing the outcome, and the costly possibility of human or mechanical error in running the experiments makes this approach inefficient for testing purposes. Mathematically modeling the growing tissue can be a useful way to augment such experimental programs because case studies can be simulated in only a fraction of the time that it takes actual tissue to grow and, once calibrated against experiments, models can be used to make predictions of optimal conditions for successful tissue growth.

A commonly-used tissue engineering protocol is to place a porous *scaffold* that has been seeded with cells into a *bioreactor* filled with a nutrient-rich culture medium. Scaffolds can have widely-varying properties, such as differing pore sizes and pore architectures, but they all serve the purpose of providing an apparatus on which cells can attach and proliferate over time. The scaffold plus cells are collectively referred to as a tissue engineering *construct*. Early mathematical models of tissue engineering took into account diffusion only and not perfusion as the mechanism of delivery of the nutrient within the culture medium. Malda et al. (2004) measured (via experiments and modeling) the development of oxygen gradients in chondrogenesis due to oxygen consumption by the cells. The goal was to predict oxygen levels within the construct to obtain an understanding of the relationship between local oxygen concentration and the oxygen demand by the cells. In an extension of this work, Lewis et al. (2005) analyzed the relationship between nutrient concentration and cell density in one spatial dimension, while assuming no cellular movement within the scaffold. They compared their model to experimental results, and showed that with proliferation, a diffusion dominated model will predict growth in the outer region of the scaffold where oxygen concentrations are highest, but less proliferation near the scaffold center where the limitations of diffusive transport mean oxygen levels are low.

One way in which nutrient may be better provided to the entire scaffold is via perfusion; that is, forced flow of nutrient-rich culture medium through the seeded scaffold. As well as the enhanced nutrient delivery due to advection, the forced flow generates fluid shear stress within the scaffold, which can stimulate enhanced cell proliferation. Certain cell types (e.g., osteoblasts) undergo enhanced proliferation when exposed to shear stress (Kapur et al. 2003; Yeatts and Fisher 2011). Raimondi et al. (2004) experimentally compared a static culture system, a surface perfused culture system (where nutrient-rich culture medium is driven only along surfaces of the scaffold), and a culture system in which nutrient-rich culture medium is forced through the whole construct. They found that there is a two-fold improvement in cell viability from forced perfusion when compared to the other methods of nutrient delivery.

They were also able to obtain details of the microarchitecture of the pores within the scaffold via light microscopy, and developed a computational fluid dynamics model to examine the modulating effect of fluid shear stress on growth. Porter et al. (2005) used microcomputed tomography to construct pore microarchitecture and used the Lattice–Boltzmann method to simulate fluid flow within the structure, in order to calculate more accurately the fluid stress in three dimensions. They found that shear stress levels leading to increased cell proliferation were lower than previously determined by Raimondi et al. (2004).

These early studies tended to focus on isolated aspects of the problem. While these analyses are very useful in improving knowledge about specific aspects of tissue growth, more recent models have moved closer to the goal of describing a tissue engineering construct in its entirety. A typical method for modeling full systems involves examining the different constituent parts as separate domains, or phases. For example, a two-phase model considers the cell population as one phase and the nutrient-rich culture medium as another phase, and considers the interactions between the two on a macroscopic level. Furthermore, there are many ways that the phases can be modeled. A simple example of this is how cell population can be considered via direct cell density or a change in scaffold permeability. Coletti et al. (2006) considered changes in both scaffold properties (due to cell proliferation) and nutrient transport (via fluid flow) in a three-dimensional perfusion bioreactor in their multiphase model. In this model, the flow external to the scaffold was governed by the Navier–Stokes equations, coupled with the Brinkman equations within the porous scaffold. Oxygen uptake was modeled by Michaelis–Menten kinetics, and cell growth as a function of nutrient concentration by the Contois equation (Contois 1959). Shakeel et al. (2011) examined the effects of initial cell seeding density and scaffold pore structure on the resulting structure of the engineered tissue construct. Chung et al. (2007) developed a three-layer model of cell proliferation, nutrient uptake, and culture medium circulation within a porous scaffold under perfusion, the scaffold itself being held between two fluid layers. In subsequent work, Chung et al. (2008) modeled only the scaffold layer, neglecting the two fluid layers, and were able to obtain the same results when compared to their earlier work.

While the above models all deal with multiple phases, the cell phase was not explicitly modeled. Instead, cells were considered as nutrient sinks and proliferation was modeled as a change of scaffold permeability and porosity. By explicitly considering a cell phase, O'Dea et al. (2008) were able to incorporate mechanotransductive effects, in particular considering the mechanical response of an imposed flow on the cell phase and predicting the resulting cell distribution. This work was expanded in O'Dea et al. (2009) to take explicit account of the scaffold and its interactions with the growing cells. The authors derived a simplified model based on an assumption of slender bioreactor geometry (i.e., a long wavelength analysis), while in a related work Osborne et al. (2010) considered a finite element solution of the full system.

A challenge still facing tissue engineers is how to initially seed the porous scaffold with the appropriate distribution of cells to obtain a desired end result. Even if the appropriate initial seeding distribution is known, it is not always possible to achieve this in the laboratory. One way around this difficulty is to exploit haptotaxis, in which cells move up gradients of a chemical that is bound to the scaf-

fold. Significant research has investigated the effects of scaffold surface modifications, in particular, how they affect cell adhesion. For example, Zelzer et al. (2012) examined how adhesion protein adsorption combined with plasma polymerized surfaces affect cell adhesion (this paper also contains a useful overview of selected earlier work on scaffold surface modification). As an alternative to adhesion proteins, great progress is being made with printing growth factors (or other biochemical signals) onto scaffolds (Campbell et al. 2005; Cooper et al. 2010; Ker et al. 2011; Miller et al. 2006, 2011). Printing growth factors onto biomaterial scaffolds offers significant advantages over allowing the growth factor to diffuse in the culture medium (Bussolino et al. 1992) since its spatial patterning is highly controllable. Such experimental studies are the main motivator for the present work, in which we model the effect of a nondiffusible growth factor bound to the scaffold. Cells seeded on the scaffold respond haptotactically to gradients of the growth factor, and undergo enhanced proliferation where growth factor is present. Campbell et al. (2005) and Miller et al. (2006) examined the cellular response to patterned growth factor: Both studies saw significantly higher cell densities in regions on which growth factor was bioprinted but, due to the growth-factor patterns used (in which concentration gradients were almost everywhere small), were unable to conclude with certainty whether haptotaxis might play a significant role (though they suspect it does not).

While much work has been done modeling cell motility and cell proliferation as they relate to tumor growth (Tao 2011), morphogenesis (Maini 1989; Oster et al. 1983; Perelson et al. 1986), and tumor-related angiogenesis (Orme and Chaplain 1996), these phenomena have yet to be fully considered from a tissue engineering perspective. In this paper, we derive a very versatile two-phase model, with one phase the cells and the other the culture medium, describing cell proliferation and transport in a porous scaffold perfused with nutrient-rich culture medium (see the schematic in Fig. 1). The model domain consists of the rigid scaffold, with perfusion driven by upstream and downstream boundary conditions. The fluid flow through the scaffold is governed by Darcy's law. Cell density is monitored as proliferation occurs, and the effect of this on the flow is captured via a change in the scaffold permeability, which also changes the pore volume fraction. Cells proliferate due to nutrient uptake, and we also take into account increased cell proliferation at moderate levels of fluid shear stress while allowing for the possibility that excessive shear stress can reduce cell proliferation. The model permits different basic nutrient types to be considered; for example, nutrients that become toxic in excess, and those that do not. Nutrient is transported by advection and diffusion (we show advective transport to dominate in all relevant parameter regimes). Cell proliferation due to nutrient uptake, and the nutrient uptake itself, are modeled by the same basic functional form, reflecting the assumption that the new cell mass created is proportional to the amount of nutrient consumed. The cells move within the scaffold via cellular diffusion in response to overcrowding and a small advective velocity (proportional to the speed of the fluid flow; essentially, a fluid drag). Finally, we add a haptotactic component to the cellular flux to model the effect of a non-diffusible growth factor bound to the scaffold. This growth factor is also assumed to enhance proliferation (Miller et al. 2006), reflected in a supplemental growth term in our cell density equation.

This paper is laid out as follows. In Sect. 2, we describe the basic dimensional model, followed by a general nondimensionalization of the model in Sect. 3. In

Sect. 4, we discuss the assumptions made in determining the various functional relationships encountered in the system of equations, e.g., relationships between permeability and porosity/void fraction, pore size, and local cell density, as well as estimation of shear stress and growth factor enhanced proliferation. The model is summarized and parameters, boundary conditions, and initial conditions are discussed in Sect. 5. Numerical methods and results are given in Sect. 6, and we conclude with a discussion in Sect. 7.

2 Model Formulation

We begin by formulating a fully dimensional model, in which asterisks denote dimensional quantities. The experimental set-up is sketched in Fig. 1 where the scaffold domain is a square two-dimensional Cartesian grid with $\boldsymbol{x}^* = (x^*, y^*)$ in which culture medium flows from $x^* = 0$ to $x^* = L^*$ with fixed impenetrable walls at $y^* = 0$, $y^* = L^*$. Time is denoted by t^*. Dependent variables in general depend on both space and time: but except where we wish to emphasize this dependence we will suppress it, for brevity. The culture medium flows at velocity $\boldsymbol{u}^*$ and pressure p^* according to Darcy's law, where the scaffold permeability is a function of c^*, the local cell density. The culture medium contains nutrient at a concentration n^*. The nutrient concentration is governed by an advection-diffusion-reaction equation with advective velocity $\boldsymbol{u}^*$ and an uptake term (sink) due to nutrient consumption by the cells. We model the cell density c^* by considering basic mass conservation principles, incorporating proliferation (source) terms due to the nutrient consumption (with shear stress dependent growth rate) and local growth factor concentration. We also account for cell death, which may in practice be due to several factors (natural death, death due to locally low nutrient concentration, death due to excessively high local shear, etc.). The growth factor concentration, ρ^*, is governed by an ordinary differential equation

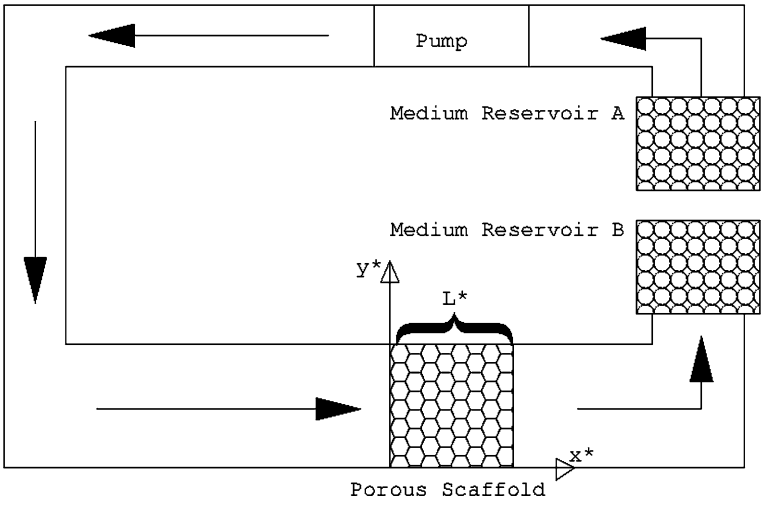

Fig. 1 A basic schematic describing the experimental set-up being modeled

which models its evolution as it is used up by cells. We discuss each of the model components in more detail below.

Fluid Flow The culture medium forced through the seeded porous scaffold is assumed to be a Newtonian fluid with (constant) viscosity μ^*. The scaffold permeability, k^*, will change as cells proliferate and fill the pores, thus we take k^* to be a function of local cell density: $k^*(c^*)$. We assume Darcy's law

$$\boldsymbol{u}^* = -\frac{k^*(c^*)}{\mu^*}\nabla^* p^*, \tag{1}$$

where $\boldsymbol{u}^*$ is the flow velocity and p^* is the pressure. The continuity (incompressibility) equation is

$$\nabla^* \cdot \boldsymbol{u}^* = 0 \tag{2}$$

which gives

$$\nabla^* \cdot \left(k^*\left(c^*\right)\nabla^* p^*\right) = 0. \tag{3}$$

This equation must be coupled to a model for c^*, and suitable boundary conditions imposed on the pressure (or the velocity).

Nutrient Concentration The culture medium transfers nutrient to the cells within the scaffold, and also (via the local fluid dynamics) exposes the cells to shear stress, which we assume affects the local proliferation rate and hence the nutrient uptake rate. The concentration of nutrient in the culture medium, n^*, satisfies an advection-diffusion-reaction equation,

$$n^*_{t^*} + \boldsymbol{u}^* \cdot \nabla^* n^* = D^* \nabla^{*2} n^* - \theta^* g^*\left(n^*, c^*, \tau_s^*\right), \tag{4}$$

where subscripts t^* denote partial differentiation with respect to t^*. The nutrient is advected with the local flow velocity; it simultaneously diffuses (with diffusion coefficient D^*) and is consumed (by the cells) at a rate (θ^*) that is modulated according to the consumption function $g(n^*, c^*, \tau_s^*)$ by both n^* and c^*, as well as by shear stress τ_s^* due to the local fluid dynamics.

Cell Density The cell density $c^*(\boldsymbol{x}^*, t^*)$ satisfies

$$c^*_{t^*} + \nabla^* \cdot \boldsymbol{J}^*_c = \lambda^* g^*\left(n^*, c^*, \tau_s^*\right) - \nu^* c^* + \gamma^* c^* f\left(\rho^*\right), \tag{5}$$

where $\boldsymbol{J}^*_c$ denotes the cell flux. In the first source term, $g^*(n^*, c^*, \tau_s^*)$, represents cell proliferation due to nutrient uptake, with rate constant λ^*. In the second source term, $f(\rho^*)$ is proliferation due to a local nondiffusible growth factor concentration, $\rho^*(\boldsymbol{x}^*, t^*)$, with an associated growth rate, γ^*, also assumed constant. The cell density c^* is included in this term because we do not expect any supplemental growth due to growth factor if there are no cells present to use it. The sink term represents natural cell death, where the death rate, ν^*, in this model is assumed to be constant.

The flux term, $\boldsymbol{J}_c^*$, accounts for advective flux due to fluid drag experienced by cells; diffusive flux, the cells' natural response to overcrowding; and haptotactic flux, the cells' response to a local growth factor gradient. Thus, the flux term is defined as

$$\boldsymbol{J}_c^* = \boldsymbol{u}_c^* c^* - D_c^* \nabla^* c^* + \alpha^* c^* \nabla^* \rho^*. \tag{6}$$

Here, $\boldsymbol{u}_c^* = \delta \boldsymbol{u}^*$ is the cellular advective velocity, assumed proportional to the fluid velocity, modeling simple dragging of cells through the scaffold by the local fluid flow (with $\delta \ll 1$ referred to as the "drag coefficient"), D_c^* is the cellular diffusion coefficient, and α^* is the haptotactic coefficient. The form of the haptotactic flux is well known; see, e.g., Murray (1989).

Growth Factor Growth factor is printed onto the scaffold, and we assume that it binds and does not undergo any advection due to flow, nor diffusion. The local concentration of growth factor is assumed to decrease at a rate dependent on local growth factor concentration and the local cell density, which leads to

$$\frac{\partial \rho^*}{\partial t^*} = -\psi^* c^* \rho^*, \tag{7}$$

where ψ^* is a constant dimensional parameter capturing the rate at which growth factor is consumed by the cells.

3 Nondimensionalization

Before we propose specific functional forms for $g^*(n^*, c^*, \tau_s^*)$, $k^*(c^*)$, etc., we nondimensionalize the system (1)–(7). This process leads to the identification of several dimensionless parameters; in some cases, these parameters will be small, enabling us to simplify the model by neglecting certain terms. We nondimensionalize as follows:

$$\boldsymbol{x}^* = L^* \boldsymbol{x},\ t^* = t/\lambda^*,\ k^*\left(c^*\right) = k_s^* k(c), \tag{8}$$

$$\boldsymbol{u}^* = u_0^* \boldsymbol{u},\ p^* = \frac{\mu^* L^* u_0^*}{k_s^*} p,\ n^* = n_0^* n,\ c^* = c_0^* c,\ \rho^* = \rho_0^* \rho, \tag{9}$$

$$g^*\left(n^*, c^*, \tau_s^*\right) = c_0^* g(n, c, \tau_s). \tag{10}$$

Lengths are nondimensionalized with respect to the length of the scaffold domain, L^*. We have chosen $(1/\lambda^*)$, the rate of cell proliferation, as the representative timescale, appropriate for analyzing the long times over which cells proliferate. The velocity scale, u_0^*, is defined as the pump flow rate, U_0^*, divided by the length scale ($u_0^* = U_0^*/L^*$), and is discussed further in Sect. 5. The pressure scale comes from balancing the terms in Darcy's law (1), where k_s^* is the permeability of the unseeded scaffold (assumed constant). Nutrient concentration and cell density are non-dimensionalized with the nutrient value at the inlet, n_0^* (assumed constant), and a representative cell density, c_0^*. The growth/uptake function g^* is also nondimensionalized via c_0^*, and the growth factor concentration by a representative value, ρ_0^* (determined in practice by an experimentalist). The resulting dimensionless model is summarized below.

Fluid Flow Darcy's law (1) and the continuity equation (2) are

$$\boldsymbol{u} = -k(c)\nabla p \quad \text{and} \quad \nabla \cdot \boldsymbol{u} = 0. \tag{11}$$

Nutrient Concentration The dimensionless form of Eq. (4) is

$$\epsilon n_t + \boldsymbol{u} \cdot \nabla n = D\nabla^2 n - \theta g(n, c, \tau_s), \tag{12}$$

where $\epsilon = (L^*\lambda^*)/u_0^*$, $D = D^*/(u_0^* L^*)$, and $\theta = (\theta^* L^* c_0^*)/(u_0^* n_0^*)$. From typical experimental data (Obradovic et al. 2000), we have significant cell proliferation over the first 5 to 7 days, and we choose a characteristic fluid velocity of 5 cm/s (see Table 2 in Sect. 5) and a characteristic length of 1 cm. Working with $1/\lambda^* = 5$ days $= 4.32 \times 10^5$ s, we have

$$\epsilon = \frac{L^*\lambda^*}{u_0^*} = \frac{1 \text{ cm}}{5 \text{ cm/s} \cdot 4.32 \times 10^5 \text{ s}} = \frac{1}{2.16 \times 10^6} \ll 1. \tag{13}$$

We assume that θ is $O(1)$ with respect to ϵ and neglect the term of $O(\epsilon)$ in Eq. (12). As will later be seen in Table 2, the dimensionless coefficient of nutrient diffusion, D, is comparable to ϵ, hence we also neglect nutrient diffusion in the scaffold. The leading-order (quasisteady) nutrient concentration equation is then

$$\boldsymbol{u} \cdot \nabla n = -\theta g(n, c, \tau_s). \tag{14}$$

Cell Density The dimensionless form of (5) is

$$c_t + \frac{\delta}{\epsilon}\boldsymbol{u} \cdot \nabla c = D_c \nabla^2 c - \alpha \nabla \cdot (c\nabla\rho) + g(n, c, \tau_s) - \nu c + \gamma c f(\rho), \tag{15}$$

where $D_c = D_c^*/(\lambda^* L^{*2})$, $\alpha = (\alpha^* \rho_0^*)/(\lambda^* L^{*2})$, $\nu = \nu^*/\lambda^*$, and $\gamma = \gamma^*/\lambda^*$. The parameters δ (introduced just after Eq. (6)) and ϵ (defined in Eq. (13) above) are both small, but the size of the ratio δ/ϵ depends on how strongly the cells are adhered to the scaffold. We assume $\delta/\epsilon \leq O(1)$.

Growth Factor Finally, the dimensionless form of the growth factor decay equation (7) is

$$\rho_t = -\psi c \rho, \tag{16}$$

where $\psi = (\psi^* c_0^*)/\lambda^*$.

4 Model Closure: Kinetics and Permeability Functions

There are three functions whose forms are still unspecified: the cell proliferation/nutrient uptake function $g(n, c, \tau_s)$ in Eqs. (14) and (15), the permeability function $k(c)$ in Eq. (11), and the function $f(\rho)$ in Eq. (15), characterizing the effect of growth factor on proliferation rate. We address each of these functions in the following sections.

Nutrient Uptake/Cell Growth Function We use the same functional form for the nutrient uptake and cell proliferation kinetics, reflecting an assumption that cell proliferation is proportional to nutrient consumed. Since we anticipate that at low cell numbers proliferation will be proportional to the cell density, but at high cell numbers overcrowding and competition for resources will lead to saturation, we choose a logistic model for $g(n, c, \tau_s)$,

$$g(n, c, \tau_s) = G(\tau_s)c\left(1 - \frac{c}{\hat{c}(n)}\right), \tag{17}$$

where the carrying capacity, $\hat{c}(n)$, depends on local nutrient availability and $G(\tau_s)$ will be chosen to incorporate the shear stress dependence. Specific choices of $\hat{c}(n)$ can model different scenarios; we take

$$\hat{c}(n) = \frac{\hat{c}_0 n}{1 + n^2}, \tag{18}$$

which implicitly assumes that nutrient is toxic in excess (hence $\hat{c}(n) \to 0$ as $n \to \infty$). However, increasing the exponent of n in the numerator to 2 can easily incorporate nontoxicity for large nutrient levels. The coefficient $\hat{c}_0 = 10$ is chosen to allow significant cell proliferation over experimental timescales; again this is easily modified if experimental data for a particular cell type suggest a different value.

Shear Stress In addition to the obvious dependence on local nutrient concentration and cell density, we assume the cell proliferation rate to depend on the local shear stress experienced by the cells within the scaffold (Lappa 2003). Darcy's law predicts the local average fluid flow on a lengthscale that is long compared with an individual pore size but small compared with the structure as a whole, thus it does not allow for explicit computation of the shear stress at the level of an individual pore. However, once we have the local average fluid velocity $\boldsymbol{u}^*$, we can calculate the local mean pore flow speed, $|\boldsymbol{u}_p^*| = |\boldsymbol{u}^*|/\phi$, where ϕ is the local void fraction, which will be discussed shortly. From this, we can estimate the size of the shear stress (see, e.g., Whittaker et al. 2009) as

$$\tau_s^* \sim \mu^* \frac{|\boldsymbol{u}_p^*|}{d^*} = \mu^* \frac{|\boldsymbol{u}^*|}{\phi d^*}, \tag{19}$$

where d^* is the average pore size.

Permeability and Void Fraction The permeability k^* clearly depends not only on the void fraction, ϕ, but also on the shape and connectivity of the pores. Nonetheless, empirical relationships between ϕ and k^* exist for a given 'type' of porous medium (Probstein 1994). A "porous medium" with no pores ($\phi = 0$) is impermeable ($k^* = 0$); one that is entirely made up of empty pores ($\phi = 1$) is infinitely permeable ($k^* = \infty$). We choose a function that immediately satisfies these conditions

$$k^* = k_s^* \frac{A\phi^\sigma}{1 - \phi^\sigma} = k_s^* k, \tag{20}$$

where A is a dimensionless constant, k_s^* is the permeability of the unseeded scaffold, and $\sigma \geq 1$ is an exponent. Rearranging to find ϕ in terms of k, substituting in the estimate for the shear stress (19) and, in the absence of firm data on appropriate values, setting $A = 1$ and $\sigma = 2$, we find

$$\tau_s^* \sim \frac{\mu^* |\boldsymbol{u}^*|}{d^*} \left(\frac{1+k}{k} \right)^{1/2}. \tag{21}$$

Permeability and Pore Size In order to use (21) in our model, we need a relation between mean pore size, d^*, and permeability. O'Brien et al. (2007) derived an equation relating permeability of a scaffold to mean pore size (and other quantities): For our model, this relation reduces to $k^*(c^*) \propto d^{*2}$ (see also Probstein 1994). This is the relation we will use in the first approximation. Recalling Darcy's law for $\boldsymbol{u}^*$ together with the scalings introduced and setting the representative shear stress scaling as $\tau_{s0}^* \sim (|p_0^*| \sqrt{k_s^*})/L^*$ (with the representative pressure scale p_0^* implicitly defined in Eq. (9)), (21) becomes

$$\tau_s^* = \tau_{s0}^* \tau_s \sim \left| p_0^* \nabla p \right| \frac{k_s^* k(c)}{L^*} \frac{\sqrt{1+k(c)}}{\sqrt{k_s^* k(c)}} = \tau_{s0}^* |\nabla p| \sqrt{1+k(c)}. \tag{22}$$

Thus, our dimensionless shear stress estimate is

$$\tau_s \sim \sqrt{1+k(c)} |\nabla p|. \tag{23}$$

Permeability as a Function of Cell Density The final puzzle piece regarding permeability is its relation to cell density. The permeability should be such that as $c^* \to 0$, $k^*(c^*) \to k_s^*$, the permeability of the unseeded scaffold, and as $c^* \to \infty$, $k^*(c^*) \to 0$. A simple general form which satisfies these properties is

$$k^*\left(c^*\right) = k_s^* k(c) = k_s^* \frac{1}{1+c^2}. \tag{24}$$

Inclusion of Shear Stress in $g(n, c, \tau_s)$ We model the inclusion of shear stress by including a prefactor

$$G(\tau_s) = \frac{\tau_s^{1/2}}{1+\tau_s} \tag{25}$$

in our cell proliferation rate function (defined in (17)). The choice of $1/2$ exponent in the numerator follows a model of Lappa (2003) (based on experiments by Obradovic et al. (2000) showing enhanced proliferation at moderate shear stress), while the denominator ensures that excessive shear stress is ultimately detrimental to proliferation.

Growth Factor Based Proliferation, $f(\rho)$ Enhanced cell proliferation due to growth factor should be small for low concentrations of growth factor, and we assume it

saturates at high concentrations. We choose

$$f(\rho^*) = \frac{\rho^{*3}}{\rho_0^{*3} + \rho^{*3}} = \frac{\rho^3}{1+\rho^3}, \tag{26}$$

using the nondimensionalization (9). The exponent here could easily be changed to modify the dependence of proliferation on ρ, if necessary.

5 Model Summary

Table 1 summarizes the relevant independent and dependent variables and functional forms. The full dimensionless system is

$$\boldsymbol{u} = -k(c)\nabla p, \tag{27}$$

$$\nabla \cdot \boldsymbol{u} = 0, \tag{28}$$

$$\boldsymbol{u} \cdot \nabla n = -\theta g(n, c, \tau_s), \tag{29}$$

$$\frac{\partial c}{\partial t} + \frac{\delta}{\epsilon}\boldsymbol{u} \cdot \nabla c = D_c \nabla^2 c - \alpha \nabla \cdot (c \nabla \rho) + g(n, c, \tau_s) - \nu c + \gamma c f(\rho), \tag{30}$$

$$\frac{\partial \rho}{\partial t} = -\psi c \rho, \tag{31}$$

$$k(c) = \frac{1}{1+c^2}, \tag{32}$$

Table 1 Summary of variables and functional forms (functional form descriptions include equation references)

Variables	Description
Independent Variables	
(x, y)	Spatial coordinates
t	Time
Dependent Variables	
$\boldsymbol{u} = (u, v)$	Darcy velocity of culture medium
p	Pressure of culture medium
c	Cell density
n	Nutrient concentration in culture medium
ρ	Growth factor density
Functional Forms	
$k(c)$	Permeability as a function of cell density, (24)
τ_s	Shear stress, (23)
$g(n, c, \tau_s)$	Cell proliferation/nutrient uptake function, (17)
$\hat{c}(n)$	Cellular carrying capacity as a function of nutrient, (18)
$G(\tau_s)$	Shear stress dependence of cell growth/nutrient uptake, (25)
$f(\rho)$	Supplemental growth factor based proliferation, (26)

$$g(n, c, \tau_s) = G(\tau_s)c\left(1 - \frac{c}{\hat{c}(n)}\right), \tag{33}$$

$$G(\tau_s) = \frac{\tau_s^{1/2}}{1 + \tau_s}, \tag{34}$$

$$\tau_s = |\nabla p|\sqrt{1 + k(c)}, \tag{35}$$

$$\hat{c}(n) = \frac{\hat{c}_0 n}{1 + n^2}, \tag{36}$$

$$f(\rho) = \frac{\rho^3}{1 + \rho^3}. \tag{37}$$

5.1 Parameters

Representative values of required dimensional parameters are found in Table 2, and the parameters contained in the dimensionless system are in Table 3 (all dimensional values are the same as those used by Shakeel et al. (2011) for chondrocyte growth in response to oxygen unless otherwise noted).

Where dimensional parameter values were not available in the literature, we simply chose default values for the corresponding dimensionless parameters as follows. For most of our simulations, the ratio of the fluid velocity to the rate at which cells are advected (dragged) by the flow is chosen so that $\delta/\epsilon = 10^{-5}$ (cells strongly adhered to the scaffold). The dimensionless haptotactic coefficient, α, may take a wide range of values depending on the particular substrate and haptoattractant. Friedman et al. (2010) noted values between 0.001 and 1 over many different systems. Since Miller et al. (2006, 2011) believe haptotactic effects to be negligible in their experimental system, we choose a small value for the majority of our simulations, $\alpha = 0.001$ (finding observable effects nonetheless). The rate of supplemental growth due to growth factor, γ, is chosen so that it is not higher than regular growth determined

Table 2 Representative values

Scaling	Name	Dimensional value
n_0^*	Representative oxygen concentration	0.2 moles/m^3
c_0^*	Representative cell density	4×10^{17} cells/m^3
L^*	Scaffold length	0.01 m
U_0^*	Pump flow rate	5×10^{-4} m^2/s
$u_0^* = U_0^*/L^*$	Fluid velocity scale	5×10^{-2} m/s
θ^*	Maximum oxygen consumption rate	1.86×10^{-18} moles/(cell s) (Obradovic et al. 2000)
D_c^*	Cell diffusion coefficient	10^{-13} m^2/s (Obradovic et al. 2000)
λ^*	Cell proliferation timescale	2.3×10^{-6} s^{-1} (Obradovic et al. 2000)
ν^*	Natural cell death rate	3.3×10^{-7} s^{-1} (Galban and Locke 1999)
D^*	Nutrient diffusion coefficient	1.5×10^{-9} m^2/s

Table 3 Approximate dimensionless parameter values

Parameter	Formula	Dimensionless value
θ	$(\theta^* L^* c_0^*)/(u_0^* n_0^*)$	0.7
δ/ϵ	[advective drag coefficient]	10^{-5}
D_c	$D_c^*/(\lambda^* L^{*2})$	4.3×10^{-4}
ν	ν^*/λ^*	0.15
ϵ	$(L^*\lambda^*)/u_0^*$	4.6×10^{-7}
D	$D^*/(u_0^* L^*)$	6.0×10^{-6}
α	$\alpha^* \rho_0^*/(\lambda^* L^{*2})$	0.001
γ	γ^*/λ^*	0.025
ψ	$(\psi^* c_0^*)/\lambda^*$	1

by $g(n, c, \tau_s)$, and the degradation rate of growth factor, ψ, is chosen so that growth factor decays neither too slowly nor quickly in comparison to regular cell proliferation.

5.2 Boundary and Initial Conditions

We now introduce the boundary and initial conditions used to solve the system (27)–(37).

Pressure and Fluid Velocity Most experiments are run with a prescribed (usually constant) rate of fluid flow through the scaffold, therefore the most appropriate boundary condition on the flow is an imposed flux in the x-direction, with no-flux conditions on the y-boundaries. However, the problem for the fluid flow is most conveniently stated in terms of the elliptic PDE for the pressure,

$$\nabla \cdot \big(k(c)\nabla p\big) = 0 \tag{38}$$

(from Eq. (11)). If the pressure conditions at $x = 0, 1$ are known then this problem is straightforward to solve, with the additional no-flux conditions $\partial p/\partial y = 0$ on $y = 0, 1$. However, the pressure drop between entry ($x = 0$) and exit ($x = 1$) points of the domain is unknown *a priori* and, moreover, changes over time as cells proliferate in the scaffold (the pressure drop must increase as the permeability decreases to maintain a constant flow rate). We circumvent this difficulty by exploiting linearity: we solve (38) for the particular solution $\tilde{p}$ satisfying

$$\tilde{p}(0, y, t) = 1, \qquad \tilde{p}(1, y, t) = 0, \qquad \frac{\partial \tilde{p}}{\partial y}(x, 0, t) = \frac{\partial \tilde{p}}{\partial y}(x, 1, t) = 0, \tag{39}$$

with corresponding velocity $\tilde{\boldsymbol{u}} = -k\nabla\tilde{p}$, and flux $\tilde{Q}_0$, which may be calculated by

$$\tilde{Q}_0 = \int_0^1 -k(c)\frac{\partial \tilde{p}}{\partial x}\bigg|_{x=l_0} dy \tag{40}$$

where the integral is taken across any surface $x = l_0$ with $0 \leq l_0 \leq 1$. Without loss of generality (due to the no flux conditions at $y = 0,\ y = 1$ and incompressibility), we may take $l_0 = 0$. We then obtain the true fluid velocity as

$$\boldsymbol{u} = \frac{\tilde{\boldsymbol{u}}}{\tilde{Q}_0}. \tag{41}$$

A more detailed description of this rescaling is given in Shakeel et al. (2011), where the reader is directed for further reference.

Cell Density and Growth Factor The only equations requiring initial conditions are those for cell density (30) and growth factor (31). We prescribe both the initial cell density $c(x, y, 0)$ and the initial growth factor density $\rho(x, y, 0)$ on $0 \leq (x, y) \leq 1$. Typically, experimentalists try to achieve a uniform initial cell-seeding density, but this is not always easy, nor is it clear that this is the optimal strategy. Our model allows us to investigate how different initial seeding patterns evolve over time, under various experimental conditions.

The initial growth factor distribution is considerably easier to specify experimentally, as it can be bioprinted (Campbell et al. 2005; Cooper et al. 2010; Ker et al. 2011; Miller et al. 2006, 2011) onto the scaffold. Specific initial conditions for model simulations will be discussed in Sect. 6, where we investigate particularly how initial growth factor distribution affects the evolution of cell distribution over time.

We also require suitable boundary conditions for the cell density equation. We assume that there is no net flux of cells into or out of the scaffold at the upstream or downstream ends, as well as no net flux through either of the impermeable walls at $y = 0, 1$. This may not be entirely correct as the scaffold is suspended in a fluid domain, which allows for the possibility of a small flux into or out of the scaffold: nonetheless it is a reasonable assumption. With the total cell flux defined as $\boldsymbol{J}_c = (\delta/\epsilon)\boldsymbol{u}c - D_c\nabla c$, the dimensionless boundary conditions on the cell density equation at all spatial boundaries are $\boldsymbol{J}_c \cdot \hat{\boldsymbol{n}} = 0$, where $\hat{\boldsymbol{n}}$ is the outward unit normal at each boundary.

Culture Medium Assuming that fresh nutrient is supplied at fixed concentration, our nondimensionalization (9) gives the appropriate boundary condition at the inlet $x = 0$ as $n(0, y, t) = 1$.

6 Results

The model as summarized in Sect. 5 is solved numerically as described in the Appendix. Here, we describe the results of several simulations, intended to provide preliminary representations of experimental scenarios, and to demonstrate the flexibility and limitations of the model.

6.1 Comparison of the Model to Experimental Results

As noted in the Introduction, there has been promising experimental work in which fibroblast growth factor 2 is bioprinted onto scaffolds to stimulate cell proliferation (Campbell et al. 2005; Miller et al. 2006, 2011). In this subsection, we use our model to reproduce, *qualitatively*, the key observations of Miller et al. (2006), in which osteosarcoma cells are seeded uniformly onto scaffolds with different concentrations of growth factor printed uniformly onto a central square region within the scaffold. In the absence of full data (describing cell features such as death rate, diffusion coefficient, etc.) for osteosarcoma cells, we use the available data for chondrocyte growth (detailed in Tables 2 and 3) and compare the experimental images (reproduced in Figs. 2a and 2c) with theoretically-obtained contour plots of local cell density after approximately 61 hours (Fig. 2b) and 176 hours (Fig. 2d). The experimental image in Fig. 2c demonstrates clearly enhanced cell proliferation in the central square region containing growth factor after 176 hours, though the effect is not as prominent in the earlier image (Fig. 2a). We see that cells also proliferate in the region free from growth factor, but at a lower rate.

The experimental images in Fig. 2 contain the phrase "32 overprints": higher growth factor densities were obtained by printing the same area of the scaffold mul-

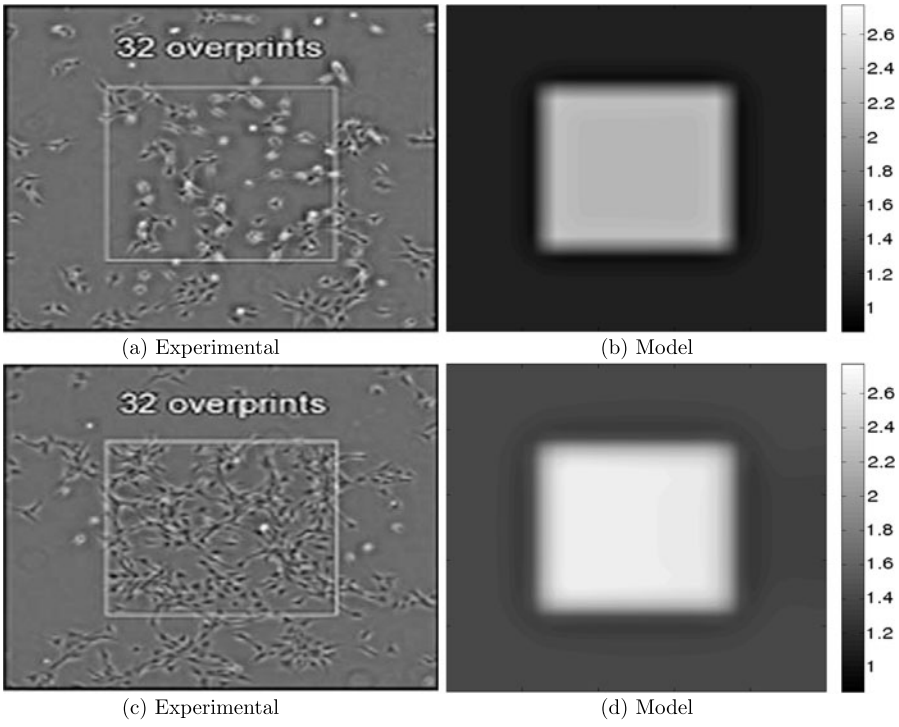

(a) Experimental (b) Model

(c) Experimental (d) Model

Fig. 2 Experimental cell density at 61 hrs (Miller et al. 2006) (**a**), and model cell density c at 61.6 hrs (**b**); experimental cell density at 176 hrs (Miller et al. 2006) (**c**), and model cell density c at 176 hrs (**d**). Model parameters from Table 3, and $\hat{\rho}_0 = 0.32$

tiple times. It is reasonable to expect that the initial growth factor density should be proportional to the number of overprints. We simulate these experimental conditions by using an initial growth factor density

$$\rho(x, y, 0) = \hat{\rho}_0\big(\tanh\big(50(x - 0.25)\big) - \tanh\big(50(x - 0.75)\big)\big) \times \big(\tanh\big(50(y - 0.25)\big) - \tanh\big(50(y - 0.75)\big)\big), \tag{42}$$

where we chose $\hat{\rho}_0 = 0.32$ (so that in principle, a value of $\hat{\rho}_0 = 1$ corresponds to 100 overprints), and an initial cell density $c(x, y, 0) = 1$.

Figures 3 and 4 show the comparison between experiment and theory as the initial growth factor density is varied. The experimental results shown are for 2, 12, 22, and 32 overprints of growth factor respectively: to mimic this in our model, we used $\hat{\rho}_0 = 0.02$, 0.12, 0.22, and 0.32. Results are compared after 61 hours (Fig. 3) and 176 hours (Fig. 4). As the initial growth factor density increases (more overprints), the experiments showed higher cell numbers in the printed region, a feature that the model reproduces. We emphasize that the comparison is not intended to be quantitative, not least because the full dataset needed to simulate correctly the experimental setup is not available. Note also that the experimental printed region is very small, making the continuum approximation for the cell density that our model employs questionable. In particular, the gradients of cell density that emerge in the simulations would not be evident in an experiment carried out on this scale. Nonetheless, the qualitative agreement obtained is encouraging.

A study of simulated total (normalized) cell population over time (Fig. 5) reveals that with higher initial growth factor densities, cells proliferated to higher final populations, as would be expected. Note that final proliferation appears to be linear in time.

The Role of Haptotaxis Despite the impossibility of making quantitative comparison, the results of the previous subsection suggest significant correlation between the experiments and our simulations. Miller et al. (2006) suggest that the primary organizational response to the growth factor by the cells is simple proliferation and not haptotactic migration. However, in these experiments, the gradients in the initial growth factor distributions are almost everywhere very small, and we therefore might not anticipate significant haptotactic movement of cells. To investigate the role of haptotaxis in our model, even with the small value of the haptotactic coefficient α used ($\alpha = 0.001$), we can run simulations in which the coefficient of the supplemental growth term in Eq. (30), γ, is set to zero, while haptotaxis is either "on" ($\alpha > 0$) or "off" ($\alpha = 0$). We use the same square growth factor distribution as previously (Eq. (42), with $\hat{\rho}_0 = 0.32$). To further demonstrate the specific effect of haptotaxis, a simulation is included in which supplemental growth due to growth factor is included, but the haptotactic effect is removed ($\alpha = 0$).

Figures 6a and 6b in which haptotaxis is "on" while supplemental growth is "off," both indicate distinct cell motility toward the center of the domain, where the growth factor is present. By contrast, Figs. 6c and 6d in which haptotaxis is "off" while supplemental growth is "on," show a smooth transition of cell density from the region without growth factor to the center of the scaffold. Figures 6e and 6f, in which the

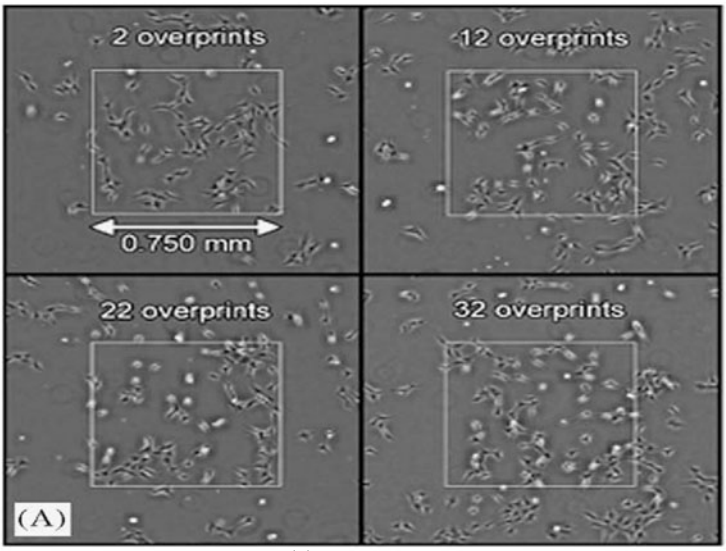

(a) Experimental

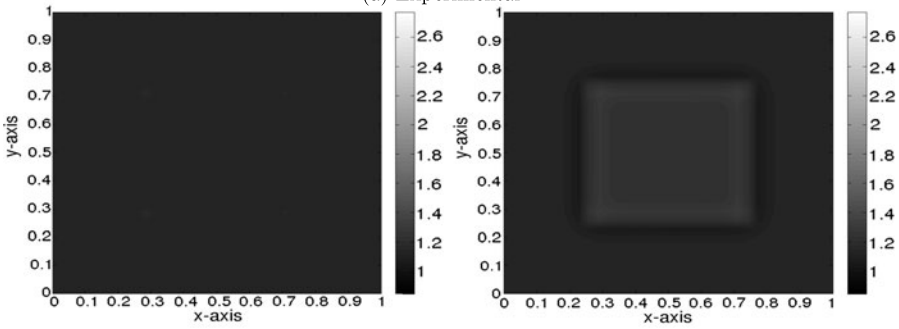

(b) Model, $\hat{\rho}_0 = 0.02$ (c) Model, $\hat{\rho}_0 = 0.12$

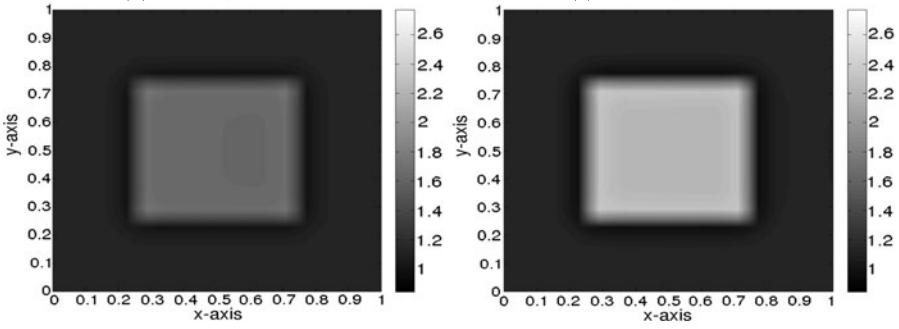

(d) Model, $\hat{\rho}_0 = 0.22$ (e) Model, $\hat{\rho}_0 = 0.32$

Fig. 3 Comparison of cell populations at 61 hrs with different initial growth factor densities: Miller et al. (2006) experiments (*upper panel*), and model simulations (*lower panels*) of cell density c, with differing values for $\hat{\rho}_0$ (other parameter values from Table 3)

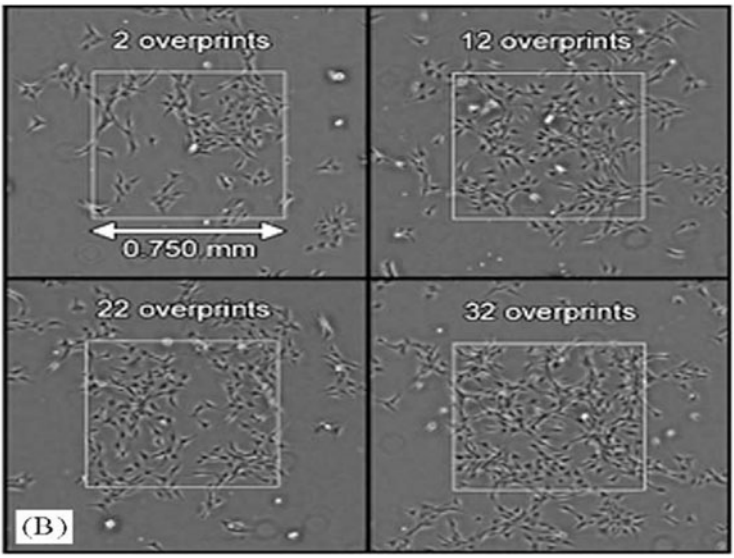

(a) Experimental

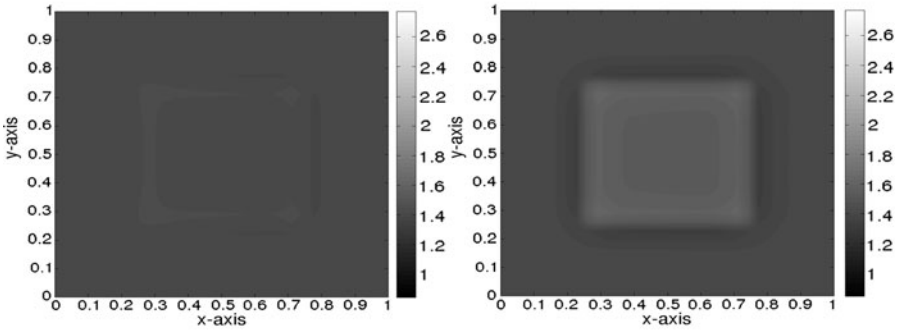

(b) Model, $\hat{\rho}_0 = 0.02$

(c) Model, $\hat{\rho}_0 = 0.12$

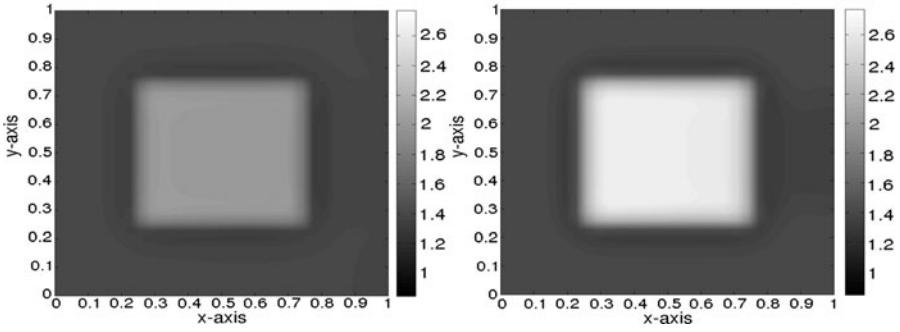

(d) Model, $\hat{\rho}_0 = 0.22$

(e) Model, $\hat{\rho}_0 = 0.32$

Fig. 4 Comparison of cell populations at 176 hrs with different initial growth factor densities: Miller et al. (2006) (*upper panel*); and model simulations (*lower panels*) of cell density c, with differing values for $\hat{\rho}_0$ (other parameter values from Table 3)

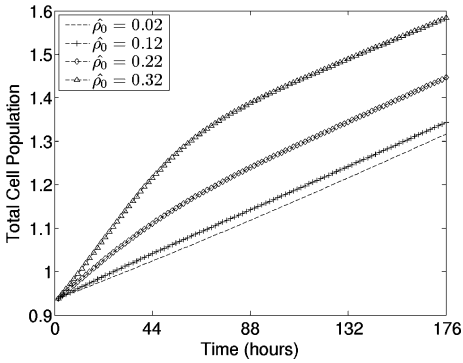

Fig. 5 Simulations of total normalized cell population for differing initial growth factor densities as seen in Figs. 3 and 4, with parameters from Table 3

growth factor is entirely passive, show a relatively uniform cell density across the domain. Together, these figures help elicit the independent effects of haptotaxis and supplemental growth.

Figure 7 shows the total (normalized) cell population in the entire domain versus time for the cases of haptotaxis and no haptotaxis (with no supplemental growth-factor-induced proliferation in both cases), and supplemental growth but no haptotaxis. The population plots indicate that the total cell population is almost unchanged by haptotaxis alone (the total population for the two simulations without supplemental growth are nearly identical over the entire course of the simulation). As expected, however, the supplemental growth has a significant effect on total cell population. Figures 6 and 7 together demonstrate that, while haptotaxis does not appear to affect the total cell population, cell migration does in fact play a role in the cell density spatial evolution in our model.

6.2 Beyond the Experiments: Further Theoretical Simulations

As observed, though haptotaxis may be playing a role in the experiments of Miller et al. (2006), its effect is hard to detect, since gradients of growth factor are small over most of the domain, and any cell migration due to the growth factor is swamped by the enhanced proliferation it stimulates. To examine more thoroughly possible effects of haptotaxis, we also simulate selected scenarios where the initial cell seeding is spatially nonuniform, and where more exotic growth factor distributions are used.

First, we assume that it is experimentally easier to seed cells on the perimeter of the scaffold than uniformly throughout. Then growth factor printed on the scaffold interior could (in principle) be used to attract cells from the periphery to the interior, giving a final cell density that is more or less uniform. Thus, we simulate this scenario, and compare to the case where no growth factor is present. We also simulate a scenario where the initial cell density is constant, but the growth factor concentration increases linearly with x and y (a uniform initial growth factor gradient). We then simulate the effects of a banded initial growth factor distribution, with various initial cell densities.

Finally, we carry out sample simulations to investigate the effects of (i) changing the haptotactic coefficient, α; and (ii) changing the cellular advective drag coefficient, δ (see Eq. (30)).

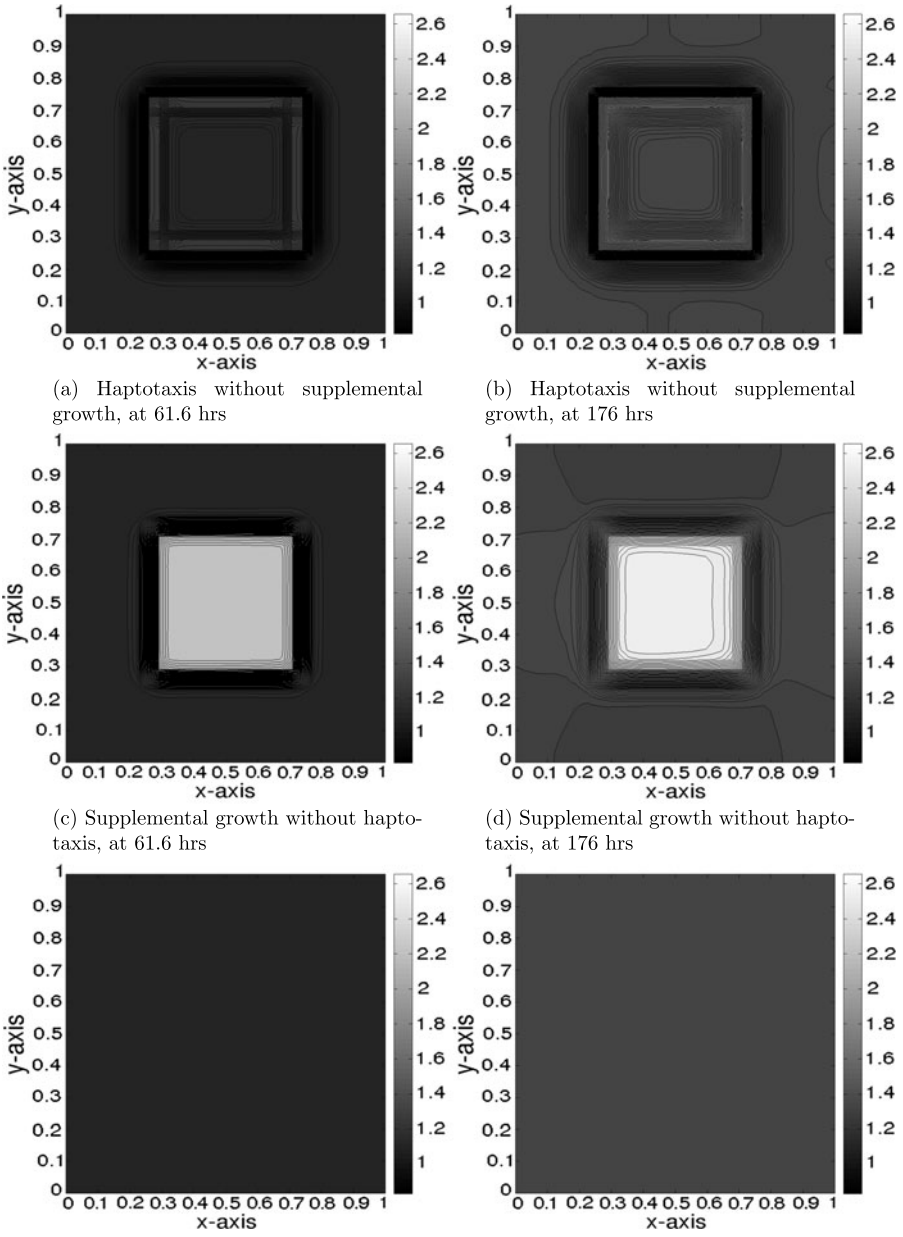

(a) Haptotaxis without supplemental growth, at 61.6 hrs

(b) Haptotaxis without supplemental growth, at 176 hrs

(c) Supplemental growth without haptotaxis, at 61.6 hrs

(d) Supplemental growth without haptotaxis, at 176 hrs

(e) No supplemental growth or haptotaxis, at 61.6 hrs

(f) No supplemental growth or haptotaxis, at 176 hrs

Fig. 6 Cell density c for simulations with: haptotaxis but no supplemental growth, $\gamma = 0$ (**a** and **b**); supplemental growth but no haptotaxis, $\alpha = 0$ (**c** and **d**); and no supplemental growth or haptotaxis, $\gamma = 0 = \alpha$ (**e** and **f**). *Contour lines* are included to accentuate the supplemental effects experienced with only haptotaxis or supplemental growth

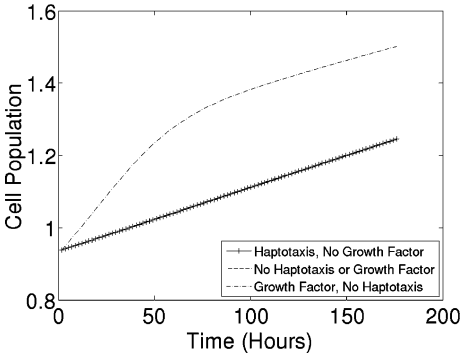

Fig. 7 Total cell population with and without haptotaxis and supplemental growth, with parameters from Table 3

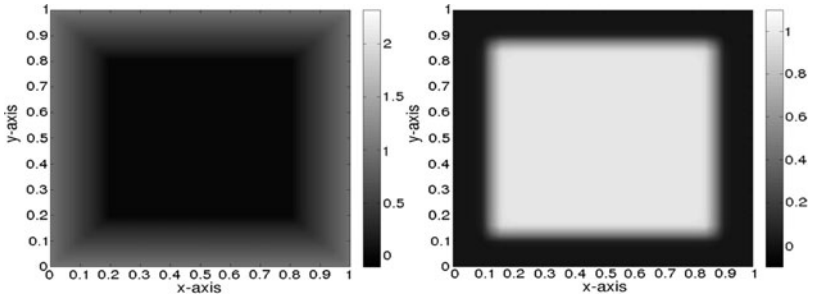

(a) Cell Density (b) Growth Factor

Fig. 8 Initial cell/growth factor distributions for simulations with peripheral cell-seeding

Peripheral Cell Seedings Here, we model a scenario where cells are seeded only on the perimeter of the domain (Fig. 8a) and migrate inward, under advection, haptotaxis (with initial growth-factor distribution as in Fig. 8b), and diffusion.

In Fig. 9, we compare model results without and with growth factor, for the initial conditions of Fig. 8. Figure 9 shows results after five (Figs. 9a and 9b) and twenty-five (Figs. 9c and 9d) days. The cell migration toward the (initially empty) center of the domain is relatively slow, due to the small values assigned to cellular advective velocity, cellular diffusive flux and haptotaxis in our model; increasing the associated parameters would give more dramatic results far sooner. A short video of this simulation is available as supplemental material on the publisher's website.

Comparison of Figs. 9a and 9c to Figs. 9b and 9d shows that inclusion of growth factor with attendant haptotaxis and enhanced proliferation significantly affects the final outcome. In particular, the cells migrate much further into the interior within the same time period when the growth factor is present, due to the haptotaxis, an effect that was not largely evident in the simulations of the experiments (with the same parameters, but different initial conditions) seen in Figs. 2–4. Figure 10 shows the total normalized cell populations over time for these simulations, and also the cell density at the center of the scaffold. It is clearly seen that the total cell population grows faster when growth factor is introduced, an effect that increases over time. This effect is even more pronounced in the center of the scaffold, as seen in Fig. 10b. The cen-

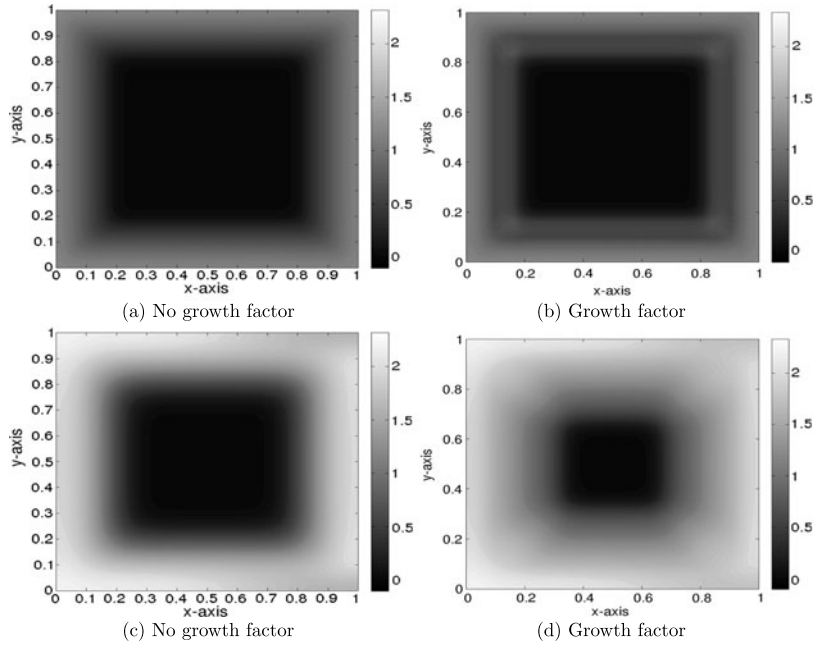

(a) No growth factor (b) Growth factor

(c) No growth factor (d) Growth factor

Fig. 9 Cell density c at 120 hrs without (**a**) and with (**b**) growth factor; and at 600 hrs without (**c**) and with (**d**) growth factor, with parameters as in Table 3

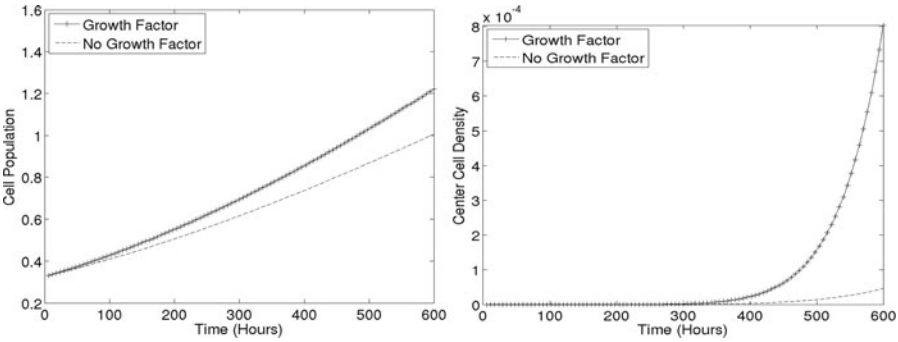

(a) Total Cell Population (b) Center Cell Density

Fig. 10 Total cell population with and without growth factor (**a**), and center cell density with and without growth factor (**b**) from simulation results shown in Fig. 9

tral cell populations in both cases are very small, but Fig. 10b provides further clear evidence that cells begin migrating to the center region much earlier when haptotaxis is included.

Linear Growth Factor Distribution To illustrate further the haptotaxis, we simulate a scenario in which a uniform (but skewed) initial growth factor gradient exists, with

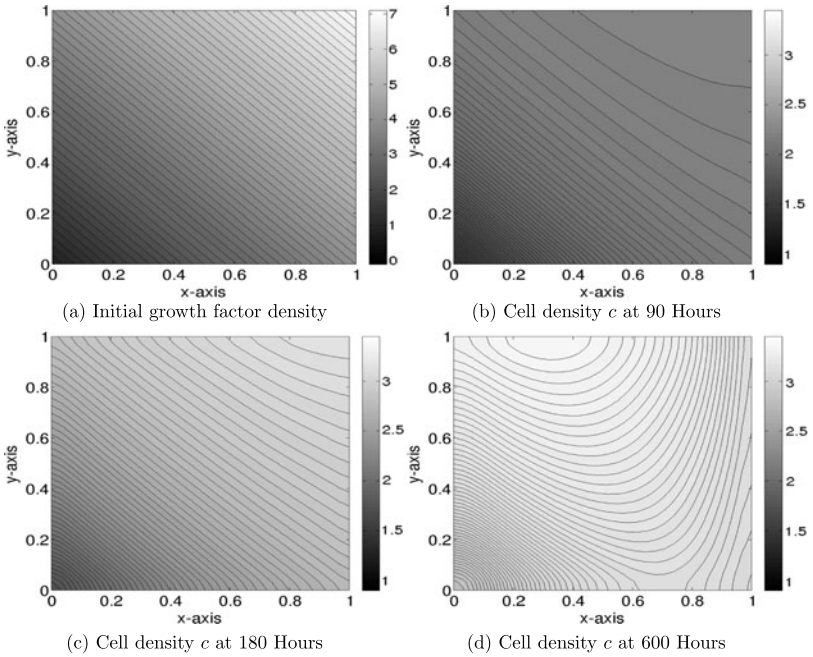

(a) Initial growth factor density (b) Cell density c at 90 Hours

(c) Cell density c at 180 Hours (d) Cell density c at 600 Hours

Fig. 11 Initial growth factor density $\rho(x, y, 0) = 3x + 3y + 1$ and cell densities after 90, 180, and 600 hrs, with parameter values from Table 3. *Contour lines* are included to clarify the differences in cell density across the domain

initially-uniform cell seeding,

$$\rho(x, y, 0) = 3x + 3y + 1, \qquad c(x, y, 0) = 1. \tag{43}$$

Results corresponding to this initial growth factor distribution are shown in Fig. 11. After 90 hours (Fig. 11b), cell density has increased everywhere in the domain, with slightly higher density near $(x, y) = (1, 1)$, which had the highest initial growth factor density. After 180 hours, the pattern of cell density across the domain closely resembles that of the original growth factor density, but by the end of the simulation (600 hrs) cell density is relatively uniform, due to the combined effects of cellular diffusion, and the higher nutrient concentration near the inlet $x = 0$. A short video of this simulation is available as supplemental material on the publisher's website.

Banded Growth Factor Printing Our final scenario illustrates the effect of a more exotic initial growth factor distribution. We consider a banded initial growth factor density,

$$\rho(x, y, 0) = \sin(6\pi x) + 1, \tag{44}$$

as seen in Fig. 12a, with three different initial cell seedings. Such bioprinting of banded growth factor (or other cellular cue) may be experimentally useful when engineering tissues which contain many different cell types, e.g., liver.

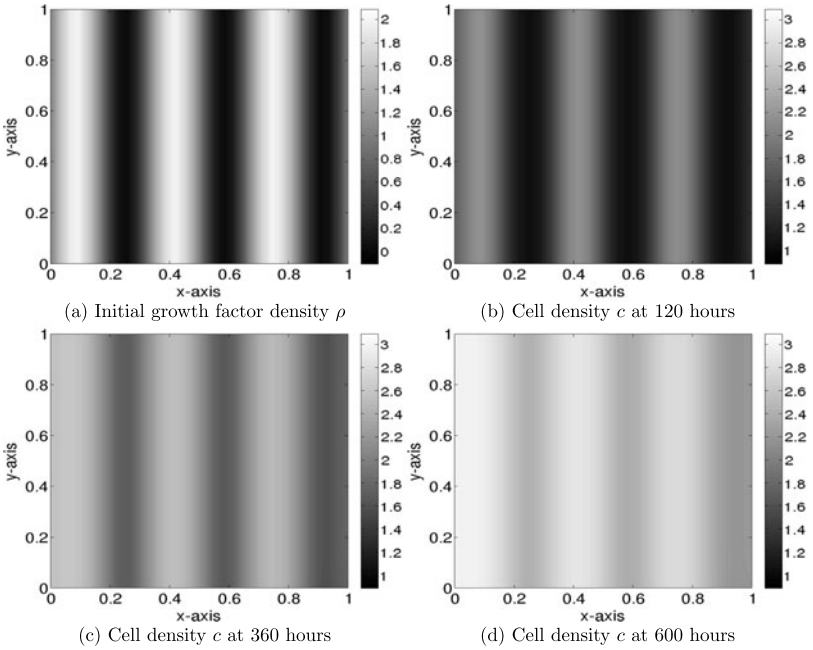

(a) Initial growth factor density ρ (b) Cell density c at 120 hours

(c) Cell density c at 360 hours (d) Cell density c at 600 hours

Fig. 12 Uniform initial cell seeding with banded initial growth factor, $\rho(x, y, 0) = \sin(6\pi x) + 1$, shown after 120, 360, and 600 hrs. Model parameters from Table 3

We first consider a uniform initial cell seeding, simulated in Fig. 12. We can clearly see in Fig. 12b that after 5 days (120 hours) the pattern of the cell density in the experiment nearly mirrors the initial growth factor density (Fig. 12a), showing significant banding. As time progresses, the banding becomes less pronounced (Figs. 12c and 12d): due to the competition from cellular diffusion and advection of nutrient throughout, the cell density rises in all areas of the scaffold (though the imprint of the initial banding is still evident).

Figures 13 and 14 show results for the same banded initial growth factor distribution (44), but with different initial cell seedings. Figure 13 shows results for peripheral initial cell seeding at all four walls of the scaffold (shown in Fig. 8a), while Fig. 14 shows results for peripheral seeding at walls $x = 0$ and $x = 1$ only. Two short videos of simulations whose results are shown in Figs. 12 and 13 are available as supplemental material on the publisher's website. Figure 13 shows an exotic pattern of cell density developing, due to the interplay between the initial growth factor pattern, the initial cell seeding, the nutrient flow, and the associated haptotactic, diffusive, and advective effects. In particular, the fully 2D nature of the initial cell-seeding here gives rise to a fully 2D final pattern. Figure 14, on the other hand, has an initial cell seeding that is nearly one-dimensional (in line with the growth factor distribution), and the final pattern that develops is correspondingly nearly 1D, and less intricate than the previous case. This limited set of examples shows that with a controllable way of printing growth factor onto scaffolds, there is great potential for creating cellular structures with detailed spatial structure.

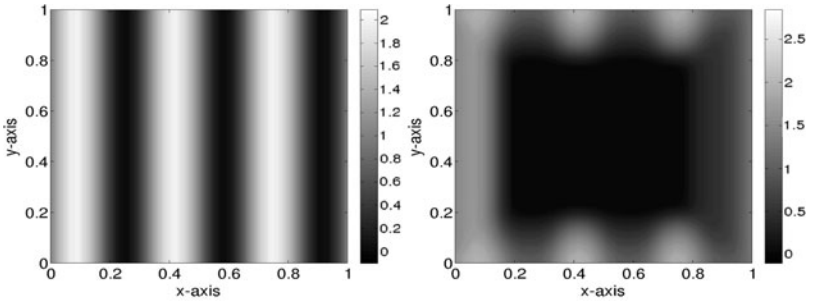

(a) Initial growth factor density ρ (b) Cell density c at 120 hours

(c) Cell density c at 360 hours (d) Cell density c at 600 hours

Fig. 13 Initial peripheral cell seeding at all four walls, with banded initial growth factor, $\rho(x, y, 0) = \sin(6\pi x) + 1$, shown after 120, 360, and 600 hrs. Model parameters from Table 3

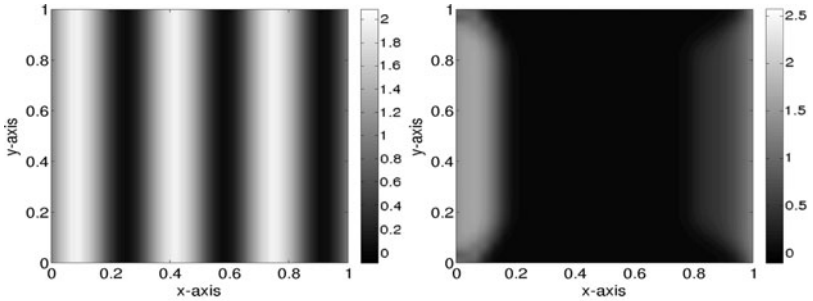

(a) Initial growth factor density ρ (b) Cell density c at 120 hours

(c) Cell density c at 360 hours (d) Cell density c at 600 hours

Fig. 14 Initial peripheral cell seeding near $x = 0$ and $x = 1$ with banded initial growth factor, $\rho(x, y, 0) = \sin(6\pi x) + 1$, shown after 120, 360, and 600 hrs. Model parameters from Table 3

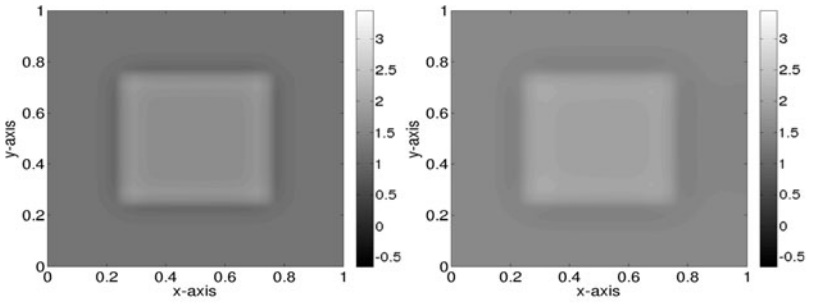

(a) Cell density c at 120 hours (b) Cell density c at 240 hours

(c) Cell density c at 480 hours (d) Cell density c at 600 hours

Fig. 15 Uniform initial cell seeding, initial growth factor density as in Eq. (42), shown after 5 (**a**), 10 (**b**), 20 (**c**), and 25 (**d**) days, with parameters as in Table 3

6.3 Varying Haptotactic and Cellular Advective Drag Coefficients α, δ

Different types of scaffold (e.g., different biomaterials, different pore structure, etc.) exhibit different cellular adhesion properties, with implications for the cell motility due to haptotaxis and fluid drag. The haptotactic cell motility would also change if a different haptoattractant was used on the scaffold. In all our simulations thus far, we have used the same values for the haptotactic coefficient, α, and the cell advective velocity factor δ. Since these parameters were chosen in the absence of solid empirical evidence, we can change them to simulate different degrees of cell motility and adhesion.

In Fig. 15, we show results of simulations with uniform initial cell seeding and initial growth factor distributed as in Eq. (42), over a period of 25 days. The original parameters of Table 3 are used; specifically, $\alpha = 0.001$ and $\delta/\epsilon = 10^{-5}$. In Figs. 16 and 17, we show the analogous results with $\alpha = 0.005$ and $\alpha = 0.01$, respectively; and in Figs. 18, 19, and 20 we show results for increased cell drag ratios, $\delta/\epsilon = 10^{-3}$, $\delta/\epsilon = 10^{-2}$, and $\delta/\epsilon = 10^{-1}$, respectively.

Figures 16 and 17 show that the increased cell motility resulting from the larger values of α is quite visible at earlier times (Figs. 16a, 16b, 17a, 17b), as the regions in the corners of the square in which growth factor was initially printed have higher cell concentrations (indicated by the lighter shades there). The evolution at later times in all simulations follows the early-time results as expected. At later times in all three simulations, proliferation has occurred throughout the entire domain (Figs. 15c, 15d,

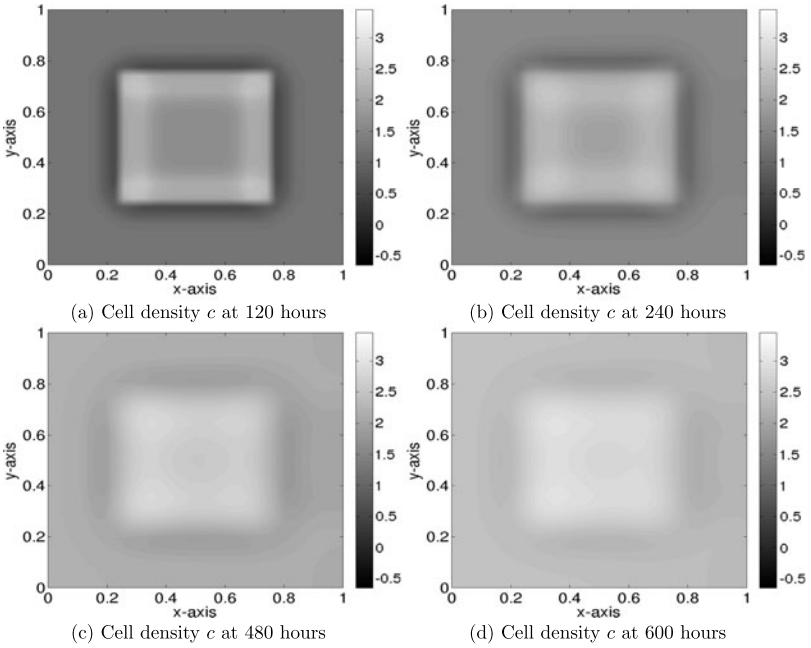

(a) Cell density c at 120 hours (b) Cell density c at 240 hours

(c) Cell density c at 480 hours (d) Cell density c at 600 hours

Fig. 16 Uniform initial cell seeding, initial growth factor density as in Eq. (42) with haptotactic coefficient, $\alpha = 0.005$, shown after 5 (**a**), 10 (**b**), 20 (**c**), and 25 (**d**) days. All other parameters as in Table 3

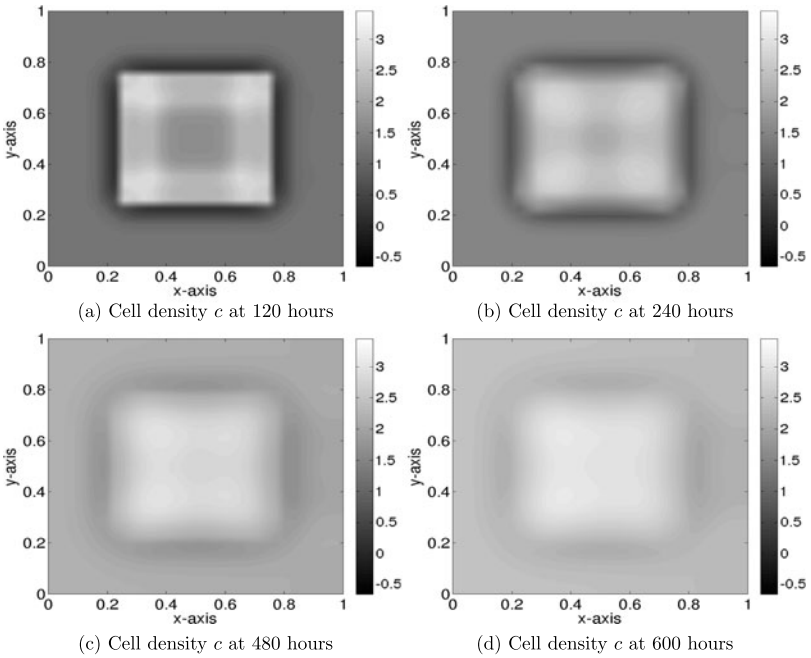

(a) Cell density c at 120 hours (b) Cell density c at 240 hours

(c) Cell density c at 480 hours (d) Cell density c at 600 hours

Fig. 17 Uniform initial cell seeding, initial growth factor density as in Eq. (42) with haptotactic coefficient, $\alpha = 0.01$, shown after 5 (**a**), 10 (**b**), 20 (**c**), and 25 (**d**) days. All other parameters as in Table 3

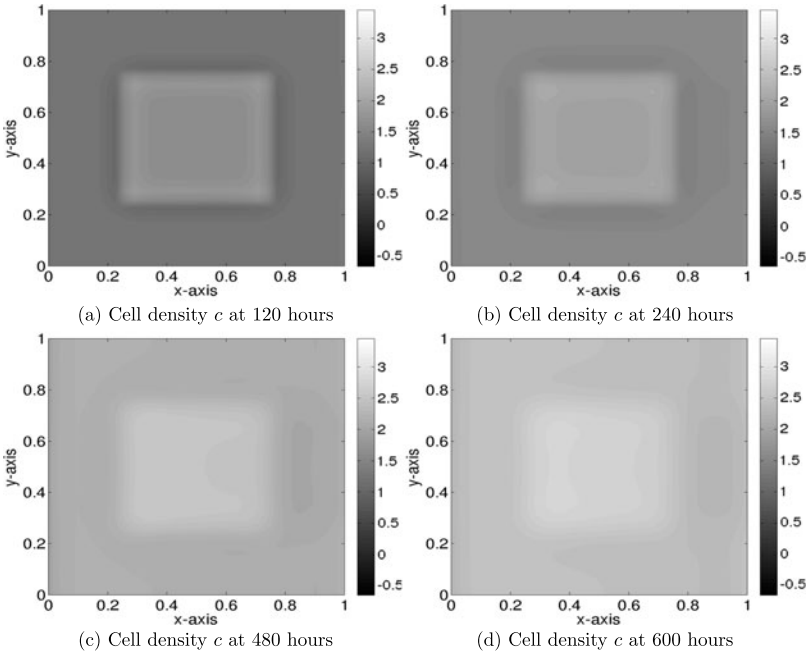

(a) Cell density c at 120 hours (b) Cell density c at 240 hours

(c) Cell density c at 480 hours (d) Cell density c at 600 hours

Fig. 18 Uniform initial cell seeding, initial growth factor density as in Eq. (42), and cellular drag parameter, $\delta/\epsilon = 10^{-3}$, shown after 5 (**a**), 10 (**b**), 20 (**c**), and 25 (**d**) days. All other parameters as in Table 3

16c, 16d, and 17c, 17d), but in the region printed with growth factor cell densities are correspondingly higher as the haptotactic coefficient increases, due to the cells migrating toward the center region faster in the early stages of the simulation.

Figures 18, 19, and 20 show analogous results as the value of the cell drag coefficient is increased. Figure 18, with δ increased by two orders of magnitude, shows little change relative to the results with the original parameter values; but Fig. 20, where δ is increased by a further two orders of magnitude, shows significant damage to the cell population. With $\delta/\epsilon = 0.1$, the cell drag velocity is only one order of magnitude smaller than the fluid velocity itself, and cellular adhesion is very weak. The cells are not only pulled to the downstream end of the domain, but as subsequent figures reveal, there is also a significant decrease in the total cell population. This is likely due to a combination of reasons: Once dragged along with the flow, the cell population is confined to a small area, where there is more competition for the available nutrient. Moreover, the relatively high cell density in that small area indicates a low permeability, with consequent high shear stresses, possibly high enough to be in the damaging regime and slowing growth.

Figures 21a and 21b show the total cell population over time as the values of α and δ/ϵ (respectively) are changed. We see in Fig. 21a that early in the simulation there is a slight up-tick in the cell population due to cells moving faster toward the region of growth factor for higher values of α, but by the end of the simulation the populations are all fairly equal. Our simulations at different α values lend credence to the concept of printing growth factor to control the final cell distribution, as Figs. 16 and 17

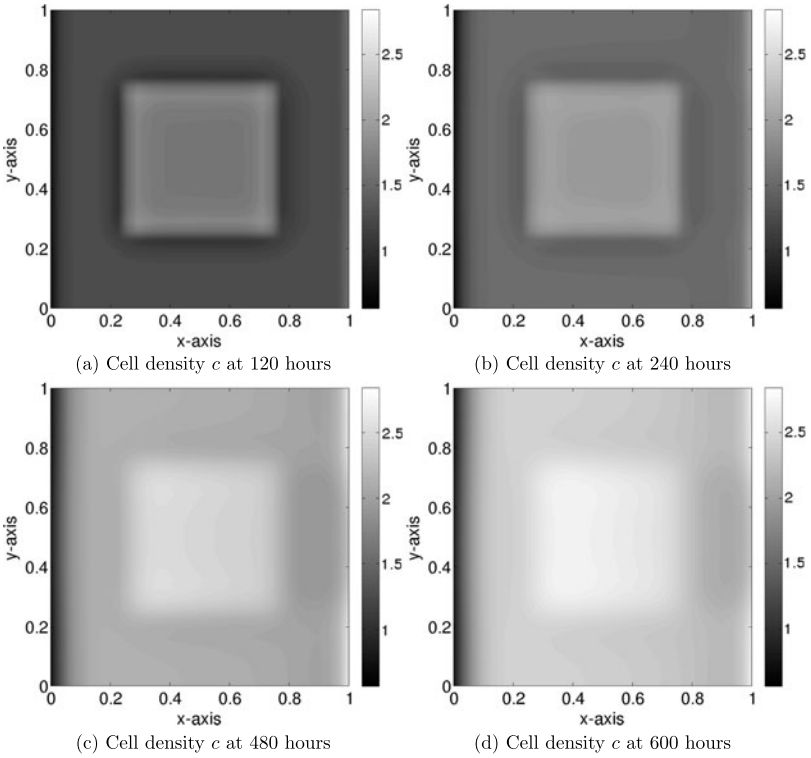

(a) Cell density c at 120 hours (b) Cell density c at 240 hours

(c) Cell density c at 480 hours (d) Cell density c at 600 hours

Fig. 19 Uniform initial cell seeding, initial growth factor density as in Eq. (42), and cellular drag parameter, $\delta/\epsilon = 10^{-2}$, shown after 5 (**a**), 10 (**b**), 20 (**c**), and 25 (**d**) days. All other parameters as in Table 3

indicate that there is a difference in the cell density distributions obtained depending on the strength of the haptotactic effect, even if the total population is unaffected (Fig. 21a). Figure 21b confirms the assessment made after examining Figs. 18 and 20, indicating that the highest drag velocity leads to a significant decrease in total cell density.

7 Discussion

The experimental results of Miller et al. (2006, 2011), and our model results presented here, demonstrate that modifying scaffold properties locally, for example by inclusion of a growth factor, can have a profound effect on the proliferation and final distribution of cells across the scaffold. Our model suggests that treating scaffolds with appropriate growth factor can increase the overall cell density distribution in regions of higher growth factor concentration, and may stimulate cell migration up growth factor gradients (haptotaxis). This effect can lead to results that differ significantly from the case where cells migrate under cellular diffusion and advection alone (see Figs. 9 and 10). We have also demonstrated the clear potential for using different patterns of initial growth factor to create specific final distributions of cells within

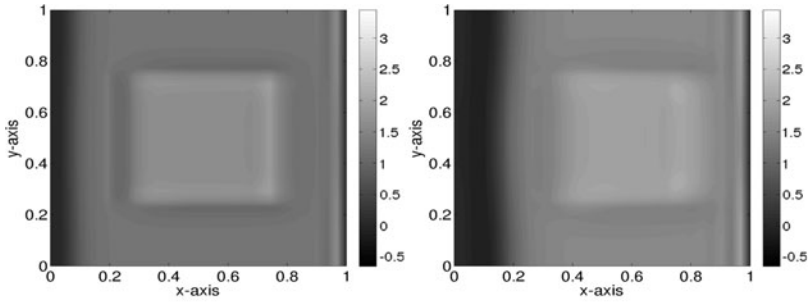

(a) Cell density c at 120 hours (b) Cell density c at 240 hours

(c) Cell density c at 480 hours (d) Cell density c at 600 hours

Fig. 20 Uniform initial cell seeding, initial growth factor density as in Eq. (42), and cellular drag parameter, $\delta/\epsilon = 10^{-1}$, shown after 5 (**a**), 10 (**b**), 20 (**c**), and 25 (**d**) days. All other parameters as in Table 3

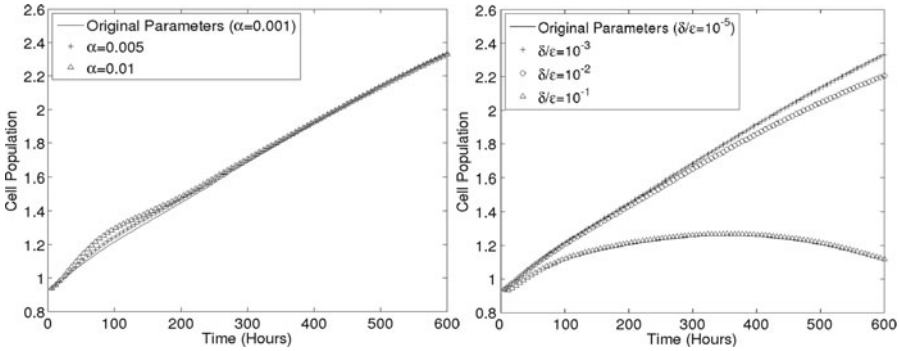

(a) Changing α (b) Changing δ/ϵ

Fig. 21 Total cell populations with different α and δ/ϵ values

a scaffold: this is backed up by firm experimental evidence, e.g., Miller et al. (2006, 2011). While only a few representative simulations are given in this paper for the purpose of illustration, when properly calibrated our model could in principle be used to predict the outcomes of many different experimental scenarios of initial cell seedings and growth factor distributions (within the limitations of our Darcy flow model and continuum approximation for the cell density).

As was seen in some of our supplemental simulations with more exotic growth factor patterning, the cell density patterns observed after several days bear the main features of the imposed initial growth factor pattern, but do not precisely mirror it. The final cell density distributions observed result from an interplay between all the effects at play: cellular diffusion and advection; proliferation due to the nutrient supply as well as the growth factor; and the haptotaxis. We believe that the limited results presented here are promising, and suggest that further experimental investigation of the haptotactic effects of growth factor in tissue engineering scaffolds are worthwhile. Such investigations would also provide more data that could be used to better estimate model parameters and functions, paving the way for more relevant simulations.

There are clear areas of indeterminacy in the model as presented here. We made a number of choices, both of functional forms and of parameters, which while phenomenologically reasonable, were not informed by solid experimental data. Nonetheless, the basic model is very flexible and easily adapted as new data becomes available. As noted in the text, it is also easily adapted to deal with different nutrient types (e.g., a nutrient that does not become toxic in excess) and different cell types (e.g., having a different mechanotransductive response to shear stress). The model is not very sensitive to the exact forms of functions such as the permeability/porosity relationship, the carrying capacity function ($\hat{c}(n)$), permeability as a function of cell density ($k(c)$), etc. We can obtain very similar results with different functional forms so long as the basic requirements itemized when originally specifying the functions are satisfied (for example, $k(c) \to 1$ as $c \to 0$ and $k(c) \to 0$ as $c \to \infty$) (Pohlmeyer 2012).

Along with the versatility of the model as remarked here, there is much that can be done to extend this work (with or without haptotactic effects). For example, no account was taken here of the toxic waste products produced by live cells, which can accumulate in regions where fluid shear is low, with damaging consequences for the cells; and no account was taken of dead cells: once dead, they are assumed to disintegrate and have no further effect. The permeability of the unseeded scaffold was assumed uniform throughout this work, but engineering a scaffold of nonuniform permeability characteristics offers yet another way of controlling the final cell distribution. Work is underway to investigate several such avenues of research.

Acknowledgements This work is supported by Award No. KUK-C1-013-04 made by King Abdullah University of Science and Technology (KAUST). The authors wish to thank Dr. Lee Weiss and Dr. Phil Campbell for use of experimental images included in this paper. J.P. would like to thank Drs. Treena Arinzeh, Shahriar Afkami, and Michael Siegel for much useful guidance with development and numerical solution of the model S.L.W. is grateful to the ERSRC for funding in the form of an Advanced Research Fellowship.

Appendix: Numerical Scheme

The first step in solving the system consists of assigning an initial cell seeding, which (via Eq. (32)) determines an initial scaffold permeability.

A.1 Pressure

Equations (27) and (28) then combine to form

$$\nabla \cdot \big(k(c)\nabla p\big) = 0, \tag{45}$$

which is solved, subject to the unit pressure drop boundary conditions (39), using a finite volume method. A sample control volume is shown in Fig. 22. The discretization for solving Eq. (45) is

$$-a_S p_S - a_W p_W + a_P p_P - a_E p_E - a_N p_N = b, \tag{46}$$

where b contains boundary data,

$$a_E = \frac{k_e}{\Delta x \delta x_e}, \qquad a_W = \frac{k_w}{\Delta x \delta x_w}, \qquad a_N = \frac{k_n}{\Delta y \delta y_n}, \qquad a_S = \frac{k_s}{\Delta y \delta y_s},$$
$$a_P = a_E + a_W + a_N + a_S,$$

and capital letters refer to points while lower case letters refer to the edge of the control volume. The discretization is set up to find solutions at the centers of boxes created by the prescribed grid, and because of this it allows for simple inclusion of the Dirichlet boundary data at $x = 0, 1$ and Neumann boundary data at $y = 0, 1$. The built-in MATLAB GMRES program is used to solve the pressure equation at the aforementioned centers of the boxes, and a MATLAB command "TriScatteredInterp" is used to extrapolate the data back onto the desired grid space. From this pressure solution, we determine the fluid velocity corresponding to a unitary pressure drop from Darcy's law, and calculate the total flux, $\tilde{Q}_0$, as in Eq. (40). We then determine the true fluid velocity in the domain via Eq. (41).

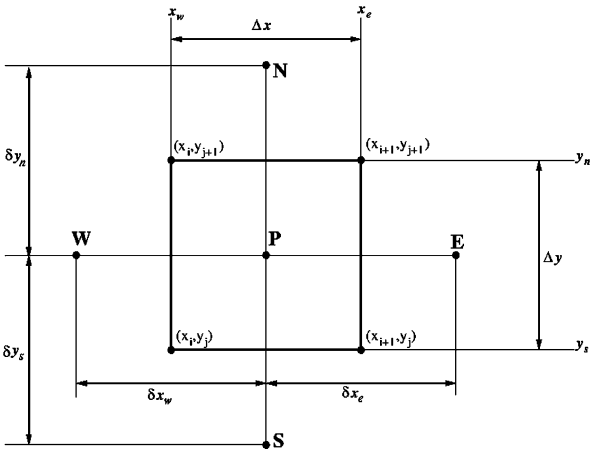

Fig. 22 Sample control volume for the finite volume method used

A.2 Nutrient Concentration

We solve for the "initial" nutrient concentration in the scaffold by solving Eq. (29) via an upwind finite difference method from $x = 0$ to $x = 1$. The method is

$$\frac{n_{i+1,j} - n_{i,j}}{\Delta x} + a_+ \frac{n_{i,j} - n_{i,j-1}}{\Delta y} + a_- \frac{n_{i,j+1} - n_{i,j}}{\Delta y} = -\theta g(c_{i,j}, n_{i,j}, \tau_{s_{i,j}}), \quad (47)$$

$$a_+ = \max\left\{\frac{v_{i,j}}{u_{i,j}}, 0\right\}, \qquad a_- = \min\left\{\frac{v_{i,j}}{u_{i,j}}, 0\right\}, \quad (48)$$

where $\boldsymbol{u} = (u, v)$. This method can be used because in all cases we consider, flow is unidirectional with respect to the x-component of the velocity, thus $u_{i,j}$ is always positive.

A.3 Cell Density

The advective drag experienced by the cells is then determined as a ratio of the fluid velocity by $(\delta/\epsilon)\boldsymbol{u}$ and the cell density is calculated at the subsequent time step using a semiimplicit ADI-type method (the nonlinear proliferation term is dealt with explicitly). The ADI-type method is

$$\begin{aligned}\frac{c_{i,j}^{t+1/2} - c_{i,j}^{t}}{\Delta t/2} &+ \frac{\delta}{\epsilon} u_{i,j} \delta_x c_{i,j}^{t+1/2} + \frac{\delta}{\epsilon} v_{i,j} \delta_y c_{i,j}^{t} \\ &= D_c\left(\delta_x^2 c_{i,j}^{t+1/2} + \delta_y^2 c_{i,j}^{t}\right) + g\left(c_{i,j}^{t}, n_{i,j}^{t}, \tau_{s_{i,j}}^{t}\right) - \nu c_{i,j}^{t}, \quad (49)\\ \frac{c_{i,j}^{t+1} - c_{i,j}^{t+1/2}}{\Delta t/2} &+ \frac{\delta}{\epsilon} u_{i,j} \delta_x c_{i,j}^{t+1/2} + \frac{\delta}{\epsilon} v_{i,j} \delta_y c_{i,j}^{t+1} \\ &= D_c\left(\delta_x^2 c_{i,j}^{t+1/2} + \delta_y^2 c_{i,j}^{t+1}\right) + g\left(c_{i,j}^{t+1/2}, n_{i,j}^{t}, \tau_{s_{i,j}}^{t}\right) - \nu c_{i,j}^{t+1/2}. \quad (50)\end{aligned}$$

This process is then repeated until the user-defined end time is attained. The solution method described is first order in time and first order in space.

References

Bussolino, F., DiRenzo, M., Ziche, M., Bocchietto, E., Olivero, M., Naldini, L., Gaudino, G., Tamagnone, L., Coffer, A., & Comoglio, P. (1992). Hepatocyte growth factor is a potent angiogenic factor which stimulates endothelial cell motility and growth. *J. Cell Biol.*, *119*(3), 629–641.

Campbell, P., Miller, E., Fisher, G., Walker, L., & Weiss, L. (2005). Engineered spatial patterns of FGF-2 immobilized on fibrin direct cell organization. *Biomaterials*, *26*(33), 6762–6770.

Chung, C., Chen, C., Chen, C., & Tseng, C. (2007). Enhancement of cell growth in tissue-engineering constructs under direct perfusion: modeling and simulation. *Biotechnol. Bioeng.*, *97*, 1603–1616.

Chung, C., Chen, C., Lin, T., & Tseng, C. (2008). A compact computational model for cell construct development in perfusion culture. *Biotechnol. Bioeng.*, *99*, 1535–1541.

Coletti, F., Macchietto, S., & Elvassore, N. (2006). Mathematical modeling of three-dimensional cell cultures in perfusion bioreactors. *Ind. Eng. Chem. Res.*, *45*, 8158–8169.

Contois, D. (1959). Kinetics of bacterial growth: relationship between population density and specific growth rate of continuous cultures. *J. Gen. Microbiol.*, *21*, 40–50.

Cooper, G., Miller, E., Decesare, G., Usas, A., Lensie, E., Bykowski, M., Huard, J., Weiss, L., Losee, J., & Campbell, P. (2010). Inkjet-based biopatterning of bone morphogenetic protein-2 to spatially control calvarial bone formation. *Tissue Eng., Part A*, *16*(5), 1749–1759.

Curtis, A., & Riehle, M. (2001). Tissue engineering: the biophysical background. *Phys. Med. Biol.*, *46*, 47–65.

Friedman, A., Aguda, B., Chaplain, M., Kimmel, M., Levine, H., Lolas, G., Matzavinos, A., Nilsen-Hamilton, M., & Swierniak, A. (2010). *Lecture notes in mathematics/Mathematical biosciences subseries: Tutorials in mathematical biosciences III: cell cycle, proliferation, and cancer*. Berlin: Springer.

Galban, C., & Locke, B. (1999). Analysis of cell growth kinetics and substrate diffusion in a polymer scaffold. *Biotechnol. Bioeng.*, *65*(2), 121–132.

Kapur, S., Baylink, D., & Lau, K.-H. (2003). Fluid flow shear stress stimulates human osteoblast proliferation and differentiation through multiple interacting and competing signal transduction pathways. *Bone*, *32*(3), 241–251.

Ker, E., Nain, A., Weiss, L., Wang, J., Suhan, J., Amon, C., & Campbell, P. (2011). Bioprinting of growth factors onto aligned sub-micron fibrous scaffolds for simultaneous control of cell differentiation and alignment. *Biomaterials*, *32*(32), 8097–8107.

Lappa, M. (2003). Organic tissues in rotating bioreactors: fluid-mechanical aspects, dynamic growth models, and morphological evolution. *Biotechnol. Bioeng.*, *84*(5), 518–532.

Lewis, M., MacArthur, B., Malda, J., Pettet, G., & Please, C. (2005). Heterogeneous proliferation within engineered cartilaginous tissue: the role of oxygen tension. *Biotechnol. Bioeng.*, *91*, 607–615.

Maini, P. (1989). Spatial and spatio-temporal patterns in a cell-haptotaxis model. *J. Math. Biol.*, *27*(5), 507–522.

Malda, J., Rouwkema, J., Martens, D., Le Comte, E., Kooy, F., Tramper, J., van Blitterswijk, C., & Riesle, J. (2004). Oxygen gradients in tissue-engineered Pegt/Pbt cartilaginous constructs: measurement and modelling. *Biotechnol. Bioeng.*, *86*(1), 9–18.

Miller, E., Fisher, G., Weiss, L., Walker, L., & Campbell, P. (2006). Dose-dependent cell growth in response to concentration modulated patterns of FGF-2 printed on fibrin. *Biomaterials*, *27*(10), 2213–2221.

Miller, E., Li, K., Kanade, T., Weiss, L., Walker, L., & Campbell, P. (2011). Spatially directed guidance of stem cell population migration by immobilized patterns of growth factors. *Biomaterials*, *32*(11), 2775–2785.

Murray, J. D. (1989). *Mathematical biology*. Berlin: Springer.

O'Brien, F., Harley, B., Waller, M., Yannas, I., Gibson, L., & Prendergast, P. (2007). The effect of pore size on permeability and cell attachment in collagen scaffolds for tissue engineering. *Technol. Health Care*, *15*(1), 3–17.

Obradovic, B., Meldon, J. H., Freed, L. E., & Vunjak-Novakovic, G. (2000). Glycosaminoglycan deposition in engineered cartilage: experiments and mathematical model. *AIChE J.*, *46*, 1860–1871.

O'Dea, R., Waters, S., & Byrne, H. (2008). A two-fluid model for tissue growth within a dynamic flow environment. *Eur. J. Appl. Math.*, *19*(6), 607–634.

O'Dea, R., Waters, S., & Byrne, H. (2009). A multiphase model for tissue construct growth in a perfusion bioreactor. *Math. Med. Biol.*, *27*(2), 95–127.

Orme, M., & Chaplain, M. (1996). A mathematical model of the first steps of tumour-related angiogenesis: capillary sprout formation and secondary branching. *Math. Med. Biol.*, *13*(2), 73–98.

Osborne, J., O'Dea, R., Whiteley, J., Byrne, H., & Waters, S. (2010). The influence of bioreactor geometry and the mechanical environment on engineered tissues. *J. Biomech. Eng.*, *132*(5).

Oster, G., Murray, J., & Harris, A. (1983). Mechanical aspects of mesenchymal morphogenesis. *J. Embryol. Exp. Morphol.*, *78*, 83–125.

Perelson, A., Maini, P., & Murray, J. (1986). Nonlinear pattern selection in a mechanical model for morphogenesis. *J. Math. Biol.*, *24*(5), 525–541.

Pohlmeyer, J. (2012). *Modeling cell proliferation in a perfusion tissue engineering bioreactor*. PhD thesis, New Jersey Institute of Technology.

Porter, B., Zauel, R., Stockman, H., Guldberg, R., & Fyhrie, D. (2005). 3-D computational modelling of media flow through scaffolds in a perfusion bioreactor. *J. Biomech. Eng.*, *38*(3), 543–549.

Probstein, R. (1994). *Physicochemical hydrodynamics, an introduction* (2nd ed.). New York: Wiley–Interscience.

Raimondi, M., Boschetti, F., Falcone, L., Migliavacca, F., Remuzzi, A., & Dubini, G. (2004). The effect of media perfusion on three-dimensional cultures of human chondrocytes: integration of experimental and computational approaches. *Biorheology*, *41*(3), 401–410.

Shakeel, M., Matthews, P., Waters, S., & Graham, R. (2011). A continuum model of cell proliferation and nutrient transport in a perfusion bioreactor. *Math. Med. Biol.* doi:10.1093/imammb/dqr022

Tao, Y. (2011). Global existence for a haptotaxis model of cancer invasion with tissue remodeling. *Nonlinear Anal., Real World Appl.*, *12*(1), 418–435.

Whittaker, R. J., Booth, R., Dyson, R., Bailey, C., Parsons Chini, L., Naire, S., Payvandi, S., Rong, Z., Woollard, H., Cummings, L., Waters, S., Mawasse, L., Chaudhuri, J., Ellis, M., Michael, V., Kuiper, N., & Cartmell, S. (2009). Mathematical modelling of fibre-enhanced perfusion inside a tissue-engineering bioreactor. *J. Theor. Biol.*, *256*(4), 533–546.

Yeatts, A., & Fisher, J. (2011). Bone tissue engineering bioreactors: dynamic culture and the influence of shear stress. *Bone*, *48*(2), 171–181.

Zelzer, M., Albutt, D., Alexander, M., & Russell, N. (2012). The role of albumin and fibronectin in the adhesion of fibroblasts to plasma polymer surfaces. *Plasma Process. Polym.*, *9*(2), 149–156.

Reproduced with permission of the copyright owner. Further reproduction prohibited without permission.